Quantifying tidal impacts on Arctic sea ice: An unexpected mechanism for the regional delay of summer melting

Kirstin Schulz,[a] An T. Nguyen,[a] Helen R. Pillar,[a] Till M. Baumann,[b] Morven Muilwijk,[c] Ilker Fer,[d] Igor Polyakov,[e] Laurie Padman,[f] Susan L. Howard,[g] and Gunnar Spreen [h]

[a] *Oden Institute for Computational Engineering and Sciences, The University of Texas at Austin, Austin, TX, United States*

[b] *Institute of Marine Research, Bergen, Norway*

[c] *Norwegian Polar Institute, Fram Centre, Tromsø, Norway*

[d] *Geophysical Institute, University of Bergen and Bjerknes Centre for Climate Research, Bergen, Norway*

[e] *University of Alaska Fairbanks, Fairbanks, Alaska, United States*

[f] *Earth and Space Research, Corvallis, Oregon, United States*

[g] *Earth and Space Research, Seattle, Washington, United States*

[h] *Institute of Environmental Physics, University of Bremen, Bremen, Germany*

This manuscript has been submitted for publication to the Journal of Physical Oceanography after minor revisions in June 2025. If accepted, the final version of this manuscript will be available via the "Peer reviewed Publication DOI" link on the right-hand side of this page and will be available open access on the publisher's website. For any question, contact Kirstin Schulz.

Corresponding author: Kirstin Schulz, kiki.schulz@utexas.edu

ABSTRACT: Tides are an important factor shaping the sea ice system in the Arctic Ocean, by altering vertical heat fluxes and advection patterns. Unfortunately, observations are sparse and the analysis of tides is complicated by the proximity of wind-driven inertial oscillations to the semi-diurnal frequencies. Furthermore, computational costs typically prohibit the inclusion of tides in ocean models, leaving a significant gap in our understanding. Motivated by summer observations showing elevated downward surface heat fluxes in the presence of tides, we analyzed simulations carried out with an eddy-permitting coupled ice-ocean model to quantify the impact of tidal effects on Arctic sea ice. In line with previous studies, we find an overall decrease in sea ice volume when tides are included in the simulations, associated with increased vertical mixing and the upward flux of heat from deeper layers of the Arctic Ocean, but this sea ice volume decrease is less pronounced than previously thought. Surprisingly, our simulations suggest that in summer, Arctic sea ice area is larger, by up to 1.5%, when tides are included in the simulations. This effect is partly caused by an increased downward surface heat flux and a consequently lower sea surface temperature, delaying sea ice melting predominantly in the Siberian Seas, where tides are moderately strong and the warm Atlantic Water core is located relatively deep and does not encroach on the wide continental shelf. Here, tidally enhanced downward heat flux from the surface in summer can dominate over the increased upward heat flux from the warm Atlantic Water layer.

SIGNIFICANCE STATEMENT: This study sheds light on the complex and understudied role of tides in Arctic sea ice dynamics. By utilizing advanced computer models, our research uncovers that, contrary to common expectations, tides contribute to a seasonal increase in sea ice area by up to 1.5% in summer. This effect is attributed to enhanced advection of sea ice into the Siberian Seas and a local increase in downward heat flux reducing sea surface temperatures, thereby delaying sea ice melting in this region. Our findings challenge prevailing notions about the negative impact of tides on sea ice and highlight the importance of incorporating tidal impacts in ocean models to improve predictions of Arctic sea ice changes, key for our understanding of both Arctic and global climate dynamics.

1. Introduction

Tides play a vital role in the Arctic climate and ecosystem. Tidal currents contribute strongly to vertical heat transport, by enhancing boundary layer turbulence created by frictional effects under the sea ice and at the sea floor, and through internal tides, formed by the interaction of barotropic tidal currents with irregular topography, especially above the continental slopes (Padman and Dillon 1991; Padman et al. 1992; Polyakov 1994; Rippeth et al. 2015; Fer et al. 2020; Schulz et al. 2021). Tidally driven mixing over the continental slope regions is estimated to contribute approximately as much to the vertical heat transport in the Arctic as double diffusion in the much larger area of the deep basins (Fer et al. 2020). Furthermore, tides fracture and transport sea ice (Nansen and Sverdrup 1898; Kwon and Lee 2016; Lemieux et al. 2018), and open and maintain ecologically important polynyas (Hannah et al. 2009). In turn, tides are influenced by the interaction with sea ice, and by changing freshwater dynamics altering stratification and hence the vertical structure of internal tides (Janout and Lenn 2014).

Despite their importance, Arctic tides are critically understudied. Disentangling tidal signals in observational data proves challenging, as the typically dominating semi-diurnal tidal constituents cannot be clearly separated in frequency space from wind-driven near-inertial oscillations in Arctic latitudes. Tides remain too computationally expensive to be included in both Arctic Ocean and global climate models in the foreseeable future (Wang et al. 2018), and the resolution of state-of-the-art climate models is nonetheless insufficient to explicitly resolve dynamics related to internal tides and associated mixing (Song et al. 2023). Neglecting tides in numerical models introduces biases, as they affect simulated vertical fluxes, the sea surface temperature field and surface heat fluxes, and even the large-scale circulation (Müller et al. 2010). For example, Holloway and Proshutinsky (2007) showed that including tides reduced the model bias of heat accumulation in the Arctic Ocean.

Previous studies on the impact of Arctic tides on sea ice found a negative effect on the sea ice mass balance, by enhancing the upward heat flux from the warm Atlantic Water layer and by opening leads and enhancing solar warming of the upper ocean in summer; and a positive effect in winter by enhancing ice mobility, allowing for the formation of more leads where new ice can easily grow (Holloway and Proshutinsky 2007). The most recent pan-Arctic modeling study on the effect of tides on sea ice, Luneva et al. (2015) with a focus on multi-decadal trends, found the dominant effect of tides to be the increase of upward vertical heat fluxes, contributing to sea ice melting and exacerbating sea ice loss trends. Regional model studies furthermore highlight the importance of residual tidal currents redistributing sea ice in the Canadian Archipelago and Baffin Bay (Kwon and Lee 2016), and a delayed freeze-up and faster ice melting by warmer sea surface temperature due to enhanced vertical mixing in the Barents and Kara Sea, with strong regional gradients (Postlethwaite et al. 2011). Based on a global model, Song et al. (2023) found tides to regionally decrease sea ice thickness, especially pronounced in the Canadian Archipelago (by 10%), when residual tidal currents export sea ice to adjacent areas.

Recent observations (Fig. 1, see section 2, Rabe et al. 2022, for details) suggest an additional mechanism for the impact of tides on sea ice, which was not considered important in the previous modeling studies listed above. In the summer of 2020, in the tidally active region around Yermak Plateau in the Atlantic sector (Fig. 2), downward surface heat fluxes under sea ice were around 2 W m^{-2}, comparable with the magnitude of the upward heat flux from the Atlantic Water layer (Schulz et al. 2021, 2024). Occasionally, these fluxes were as high as 40 W m^{-2} (Fig. 1b), presumably due to enhanced shear production associated with ice drift-shear alignment (Fig. 1a), a mechanism previously described on the Laptev Sea shelf (Lenn et al. 2011). Strong downward heat fluxes during summer can potentially lower the sea surface temperature and consequently delay the melting of sea ice, but the pan-Arctic importance of this mechanism cannot be derived from observations alone.

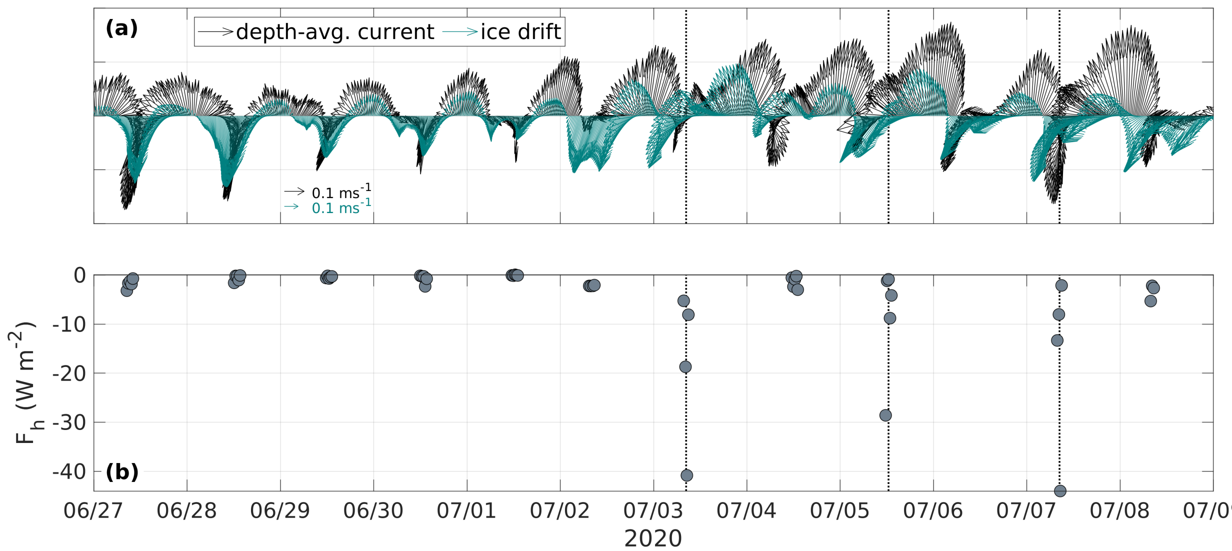

FIG. 1. (a) Quiver plots of the depth-averaged current (black) and ice drift (teal) velocity, on different scales as indicated, to illustrate the phase of tidal currents and sea ice drift. (b) Turbulent heat fluxes over the layer from surface down to the local temperature minimum located at a depth of about 35 m (W m^{-2}, negative values indicate downward fluxes, see section 2c). Vertical dotted lines are for orientation. Observations are from the region above Yermak Plateau, see Fig. 2.

In this study, we use a high-resolution coupled sea ice and ocean model of the Arctic and North Atlantic (described in section 2), run for a whole year with and without tides, to quantify the regional and seasonal variability of dominant tidal processes impacting sea ice dynamics on a pan-Arctic scale. Advanced computational resources and limiting our analysis to only a single year allow us to achieve a higher level of detail in our simulations compared to Luneva et al. (2015). Recent model developments and improved boundary and forcing conditions, taken from a data-constrained state estimate of the Arctic Ocean (Nguyen et al. 2021), provide further improvement of the results. We evaluate our model simulations against observational data in section 3 before describing the effect of tides on sea ice in sections 4 and 5, discuss the limitations of our methods and the potential consequences of our findings in section 6, and conclude the study in section 7.

2. Methods

a. Numerical Model

Simulations of the Arctic Ocean and sea ice system were based on the Massachusetts Institute of Technology general circulation model (MITgcm, Marshall et al. 1997; Adcroft et al. 2004). The grid was of the Lat-Lon-Cap (LLC) family, widely used within the Estimating the Circulation and Climate of the Ocean (ECCO) community (e.g., Nguyen et al. 2021; Flexas et al. 2019). The regional configuration, based on the LLC-1080 grid, had nominal horizontal grid spacing of about 3.5 km in the Arctic. The domain covered the Atlantic northward of the equator, the entire Arctic and its marginal seas (Fig. 2). The vertical grid comprised 90 unevenly spaced levels, with thicknesses ranging from 1 m to 25 m in the upper 300 m, increasing to 480 m in the lowest level.

Initial conditions for January 2002 were based on the World Ocean Atlas 2009 version 2 hydrography (Locarnini et al. 2010; Antonov et al. 2010) and the Pan-Arctic Ice Ocean Modeling and Assimilation System (PIOMASS, Zhang and Rothrock 2003). Lateral open boundary ocean and sea ice conditions were taken from the Arctic Subpolar gyre sTate Estimate Release 1 (ASTE R1, Nguyen et al. 2021). Atmospheric forcing was applied via bulk formulae (Large and Yeager 2008), with atmospheric state variables taken from the 3-hourly Japanese 55-year Reanalysis (JRA-55, Kobayashi et al. 2015). The applied precipitation included a correction for the known positive bias in JRA55 (Stewart et al. 2020), obtained via adjoint-based optimization of ASTE R1 (Nguyen et al. 2021). Monthly mean runoff was taken from the Arctic Runoff Data Base (ARDB, Grabs et al. 2000) with adjustments in the Arctic obtained from the Green Functions' optimization of Nguyen et al. (2011).

Tidal forcing was calculated from the astronomical gravitational tidal potential and applied as an hourly surface pressure loading term (Arbic et al. 2018; Ponte et al. 2015; Ponte and Vinogradov 2007). The full luni-solar tidal potential spectra were included. At the lateral open boundaries, additional tidal forcing was derived from the global barotropic inverse tide model TXPO8-Atlas, an update of Egbert and Erofeeva (2002). Low-mode baroclinic tides are explicitly resolved, to the limit of the horizontal and vertical resolutions of the model (Arbic et al. 2018). Smaller time steps and Crank-Nickelson barotropic time stepping were employed for improved accuracy of barotropic tides representation and energy conservation (Campin et al. 2004). No additional parameterizations of wave drag or any internal wave damping mechanisms are implemented (Arbic et al. 2018). The configuration of the MITgcm used is mass /volume and tracer conserving, and respective budgets are closed (see Appendix B in Nguyen et al. 2020, and the references therein). This study uses a linear free surface and volume-conserving configuration of the MITgcm for stability, in line with the widely utilized previous MITgcm-based global very high resolution configuration described in Arbic et al. (2018). The applied barotropic tidal velocities at the lateral open boundaries are harmonics with zero mean value and do not contribute to the accumulation of volume. Mass convergence between pairs of runs with and without tides yields minimal differences with no discernible trends.

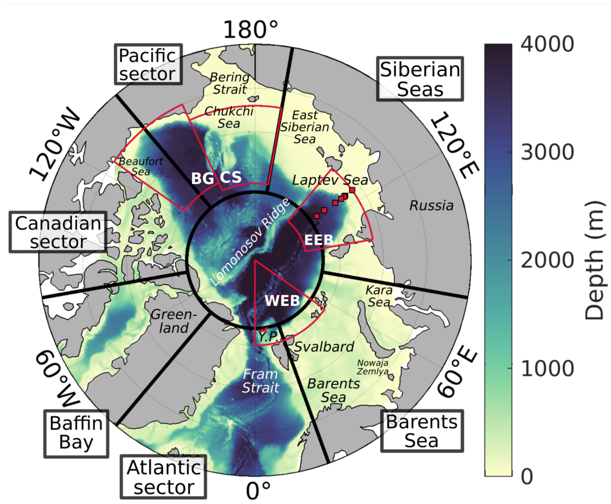

Fig. 2. Model bathymetry north of the Arctic circle, with sectors used to discriminate regional contributions indicated in black: the central Arctic Ocean north of 82°N, Baffin Bay (40°W to 80°W), the Canadian sector (80°W to 140°W), the Pacific sector (140°W to 170°E), the Laptev and East Siberian Sea (170°E to 80°E), the Barents Sea (20°E to 80°E), and the Atlantic sector (20°E to 40°W). Red squares mark the positions of the NABOS moorings; areas for the validation of the temperature and salinity profiles are marked in red (EEB = Eastern Eurasian Basin at 76–84°N, 100–140°E; WEB = Western Eurasian Basin at 80–90°N, 0–55°E; CS = Chukchi Sea at 72–81°N, 155–190°W; BG = Beaufort Gyre at 70–80°N, 125–155°W). The short red line above the Yermak Plateau (a relatively shallow expanse northwest of Svalbard, denoted as Y.P.) shows the track along which the data displayed in Fig. 1 was collected.

Vertical mixing was represented using the K-Profile Parameterization (KPP, Large et al. 1994) in the surface layer. Three dimensional interior vertical diffusivities were based on the ASTE R1 optimized combined background and parameterized diapycnal mixing fields (Nguyen et al. 2021). Background values were of O(10^{-7}–10^{-6}) m^2s^{-1}, typical for the Arctic Ocean (Fer 2009; Schulz et al. 2023a, 2024). To represent internal wave breaking over rough topography (Nikurashin and Ferrari 2013), background vertical diffusivities were enhanced by one order of magnitude, with the multiplicative enhancing factor varying linearly over a horizontal length-scale of 120 km, from 10.0 at an ocean grid point horizontally adjacent to a land point to 1.0 in the interior. The dynamic and thermodynamic interactive sea ice model was based on an evolved formulation by Semtner (1976); Heimbach et al. (2010) and Losch and Danilov (2012), featuring a viscous-plastic rheology with an elliptic yield curve and a single thickness category. Ridging is treated implicitly by limiting the sea ice concentration to a maximum of one, with further ice convergence resulting in thicker ice (Adcroft et al. 2018). The landfast ice parameterization that has recently been implemented in the MITgcm (Liu et al. 2022) was not available at the time the simulations were carried out and has not been included here. The subgrid-scale parameterization of Nguyen et al. (2009) was employed to treat mixed layer salt redistribution during sea ice formation and brine rejection to maintain realistic upper Arctic ocean stratification.

Two 1-year long simulations were performed for year 2014, one with and one without tides. The period of 2014 was selected because it offers the most comprehensive data coverage from the NABOS mooring array, located across the Laptev Sea slope (see Fig. 2 and section 2b), used for model validation. Model 2D and 3D outputs were stored every hour. During post-processing, spatial averages for sea ice properties were taken over the whole model domain, whilst ocean properties (e.g., sea surface temperature) were averaged for all grid points north of 66°N. To decompose signals into their regional contributions, we subdivided the Arctic in the non-overlapping sectors indicated in Fig. 2.

b. Observational data used for model evaluation

To assess the performance of our model (section 3), we compare the model output to observational data. For this purpose, we use temperature and salinity profiles obtained in 2014 from Muilwijk and Polyakov (2022). This dataset is an updated version of the archive created by Polyakov et al. (2020a) and contains a comprehensive collection of hydrographic observations of the Arctic Ocean from 1970 to 2017 including temperature and salinity profiles obtained from ships, aircraft, drift stations, autonomous drifters (Ice-Tethered Profilers), and submarines. We averaged the profiles over four regions (see Fig. 2) of the Arctic Ocean following Polyakov et al. (2020a). We obtained the stratification profiles from the model fields by averaging over the whole year 2014 and using the same regional boundaries. All temperature and salinity data have been converted to Conservative Temperature (°C) and Absolute Salinity (g kg^{-1}) using the TEOS-10 equation of state as implemented in the Gibbs-SeaWater Oceanographic Toolbox (McDougall and Barker 2011).

To evaluate how the Arctic boundary current and the variability of tidal currents across the continental slope are reproduced in the simulations, we use data collected in the context of the Nansen and Amundsen Basins Observational System (NABOS, https://uaf-iarc.org/NABOS/). An array of six moorings (M1$_1$–M1$_6$) along the 126°E meridian from just offshore of the Laptev Sea shelf (~77°N, 250 m water depth) to the abyssal plain (~81°N, 3900 m depth, see Fig. 2) was deployed for two years from September 2013 to September 2015 (Polyakov 2016; Baumann et al. 2018; Polyakov et al. 2020b, 2025). All moorings were designed to obtain profiles of the two-dimensional horizontal velocity over variable depth ranges. Velocities were obtained at hourly resolution for the upper ~50 m using 300 kHz Acoustic Doppler Current Profiler (ADCP) at all but two moorings: M1$_1$, where a 75 kHz ADCP moored near the seabed was used to capture velocities throughout most of the water column, and M1$_5$, which missed its target depth and was deployed ~30 m too deep. The ADCPs generally returned full 2-year data records, but the ADCP at M1$_5$ stopped working after about 10 months. Manufacturer-provided accuracies for speed and direction are ±0.5 cm s^{-1} and ±2° for vertical averaging bin sizes of 2 m and 5 m for the 300 kHz and 75 kHz ADCPs, respectively. Signals from all ADCPs were contaminated close to the surface by surface reflections of sidelobe energy. For the upward-looking 300 kHz ADCPs moored near 50 m depth, the upper 8 m could not be used; for the 75 kHz ADCP mounted at ~250 m depth at M1$_1$, the top 30 m were discarded. The NABOS mooring array was supplemented by mooring #1893, deployed in September 2013 on the Laptev Sea shelf in ~50 m water depth near 76°N, 126°E, within the German-Russian "Laptev Sea System" partnership during the Transdrift 21 expedition. The mooring was recovered and redeployed in 2014 during Transdrift 22 to obtain an additional year of data. Both deployments included an upward-looking 300 kHz ADCP at 35 m (2013) and 37 m (2014) depth, and a downward-looking, 600kHz ADCP mounted at 30 m (2013) and a 1200 kHz at 35 m (2014), respectively, to resolve the near-bottom part of the water column.

The validation of the model results with respect to the boundary and tidal currents focuses on the Siberian Seas for two reasons: First, the NABOS mooring data offers an exceptional level of detail, capturing cross-slope gradients with high spatial resolution. Second, one of main aspects discussed in this study, the regional increase in sea ice extent and thickness in the presence of tides (see section 5), emerges prominently in the Siberian Seas. To assess how the boundary current is reproduced, the hourly model and observational data is first averaged to weekly values before calculating the mean and standard deviation (Fig. 4), to exclude tidal and other short term variability. Winter and summer averages refer to the two-month periods of January and February, and June and July, respectively, to match the chosen periods to discuss sea ice anomalies in the model results (section 4). Before calculating the root mean square current velocity anomaly shown in Fig. 6c, we removed the weekly averaged background current from the depth-integrated velocity time series. To calculate the rotary spectra shown in Fig. 7, we applied Welch's method with window length of 6 months and 50% overlap to the depth-averaged velocities at the original hourly resolution.

c. Observational data shown in Fig. 1

Data shown in Fig. 1 (section 1) were obtained during the Multidisciplinary drifting Observatory for the Study of Arctic Climate (MOSAiC) campaign over Yermak Plateau and in the Fram Strait (Rabe et al. 2022). Profiles of turbulent dissipation rates ε (W kg^{-1}) at 1 m vertical resolution were estimated from the shear-probe records from a free-falling, tethered microstructure profiler (MSS90L, Sea & Sun Technology, Germany). The profiler was operated through a hole drilled in the sea ice, at a minimum distance of 250 m from the research icebreaker *Polarstern*. Profiles were collected on a near-daily basis, details on the measurement setup and processing can be found in Schulz et al. (2022a). Measured dissipation rates in the upper 50 m of the Yermak Plateau region are well above the instrument's noise level (see Fig. 7 in Schulz et al. 2024). Horizontal current velocity and sea ice drift velocity were taken from an RD Instruments 75 kHz ADCP co-located with a GPS compass (Baumann et al. 2021). The ADCP was deployed through the sea ice with transducers facing downward.

Heat fluxes in the water column were calculated as described by Schulz et al. (2023a): The vertical diffusivity K_z (m^2 s^{-1}) is calculated from ε and density profiles following Bouffard and

Boegman (2013), accounting for possibly different turbulent regimes and stratification ranges. Averages of turbulence quantities such as ε and K_z are calculated using the maximum likelihood estimator (MLE, Baker and Gibson 1987). Vertical heat fluxes over the vertical interval from 4 m depth to the temperature minimum between 20 and 40 m are calculated from the mean vertical gradient in potential temperature $\frac{\partial\theta}{\partial z}$ over that layer, according to

$$F_h = -\rho_0 c_p K_z \frac{\partial\theta}{\partial z}, \tag{1}$$

where $\rho_0 = 1027$ kg m^{-3} is the reference density, and $c_p \approx 3,991.9$ J kg^{-1} K^{-1} is the specific heat capacity of seawater. Values were excluded when the near-surface stratification over the same depth interval was weak, identified as $N^2 < 3\times10^{-5}$ s^{-2}, with N^2 being the Brunt–Väisälä frequency. Positive values indicate upward heat fluxes.

3. Model evaluation

a. Stratification and Boundary Current

Our model simulations reproduce the vertical structure of temperature and salinity stratification reasonably well (Fig. 3). The vertical position of the warm subsurface layer of Atlantic or Pacific origin as well as the shallower near-surface temperature maximum in the Beaufort Gyre formed locally by summer heating (e.g., Steele et al. 2011) are accurately captured. A warm temperature bias exists in the Eurasian basins and Chukchi Sea, related to difficulties in accurately reproducing the Atlantic Water pathway, a common issue in climate models (Heuzé et al. 2023; Wang et al. 2023), and an underestimation of vertical heat fluxes from the Atlantic Water layer. This bias is more pronounced when tides are included in the simulations, which might partially be associated with changes in lateral advection when tides are present (Fig. 4). These biases are also present in ASTE R1, despite extensive optimization to reduce the misfit to a large set of satellite-based and in-situ observational constraints, and are attributed to the low observation density in the Eurasian Basin as well as highly unconstrained iso- and diapycnal mixing estimates (Nguyen et al. 2021). Compared to observations, model simulations are fresher in the upper 100 m in the Eurasian basins, and saltier in the upper 300 m in the Chukchi Sea and Beaufort Gyre. However, our model exhibits minimal salinity biases compared to other climate models, and, most relevant for our study,

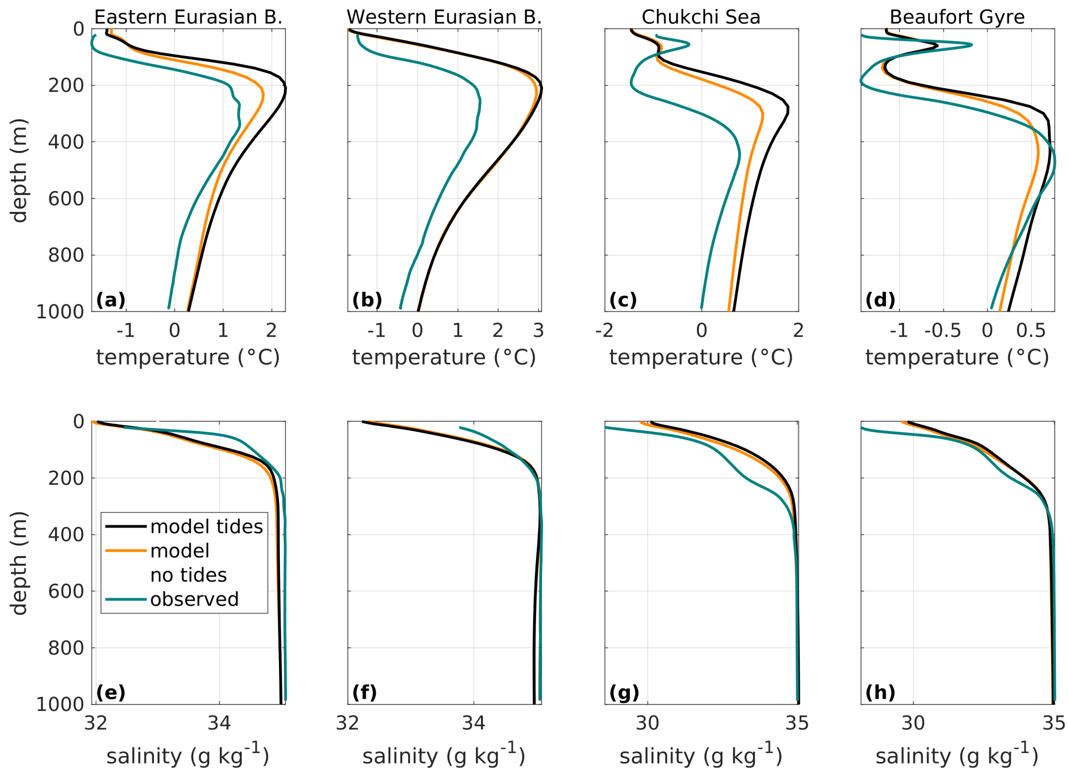

FIG. 3. Annual mean profiles of (a)-(d) Conservative Temperature (°C) and (e)-(h) Absolute Salinity (g kg^{-1}) in four regions of the Arctic Ocean indicated in red in Fig. 2. Teal lines are observations from Muilwijk and Polyakov (2022); black lines indicate simulated results from the model run including tides; orange lines the simulated results excluding tides, averaged over the same regions.

accurately captures the steepness of the salinity gradient, which ultimately dictates the strength of stratification with direct influence on the magnitude of vertical heat fluxes.

The cross-slope profile of the simulated Arctic boundary current is also in good agreement with observations from NABOS moorings (Fig. 4). In summer (data not shown), simulations including tides produce a slightly slower boundary current that is more confined to the upper slope, but the difference between the model runs is small. The good reproduction of the boundary current at this location may be partially attributed to the assimilation of the NABOS mooring data in the ASTE R1 solution (Nguyen et al. 2021), which served as the foundation of the model configuration used here. This is, however, not necessarily expected due to the inclusion of a vast amount of other data in ASTE's misfit cost function and limitations imposed by model representation error. Furthermore,

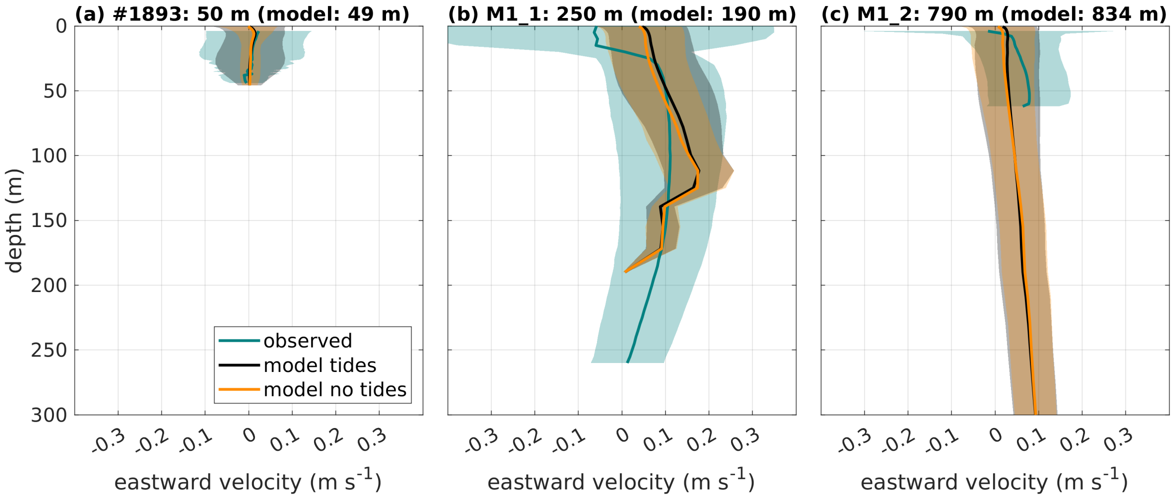

FIG. 4. Annual mean profiles of the eastward (along-slope) velocity across the continental slope of the Laptev Sea at 126°E, with mooring location depth (corresponding model grid point depth) as indicated. Teal lines are observations from the NABOS mooring array, black lines indicate results for the simulation including tides, orange lines indicate results from the simulations excluding tides. Shading indicate the respective standard deviation.

the closest model grid point to NABOS mooring $M1_1$ (i.e., the model grid point along the 126°E transect with closest matching water depth) is approximately 200 m deeper than the mooring location, which likely introduces some bias and also illustrates that accurately simulating processes above the steep continental slope requires an even finer spatial grid resolution.

The vertical structure and small amplitude of the current velocities on the shelf are especially well-captured, and amplitude and variability of the boundary current core at the upper continental slope are in good agreement, whilst the smaller offshore current velocities are slightly underestimated in the simulations (Fig. 4). The vertical structure of the boundary current above the upper continental slope is somewhat misaligned, with the velocity maximum being located further down in the water column compared to the observations. This bias appears to be stronger in summer, when the observed vertical structure of the boundary current is fairly homogeneous, except for a strong westward component and a large variability in the upper 30 m, which are absent in the simulations (data not shown). Observations and model results agree considerably better in winter. Overall, the position and strength of the boundary current are fairly well reproduced.

b. Tides

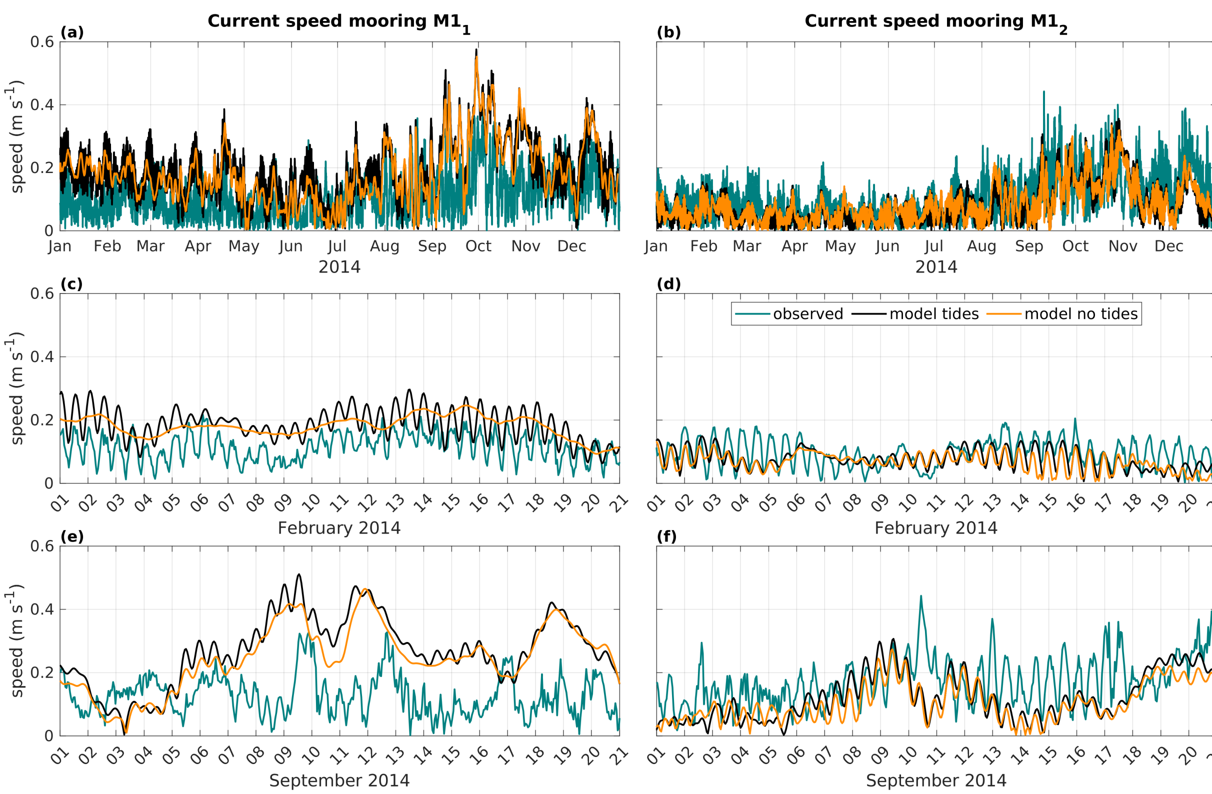

FIG. 5. Time series of the depth averaged current speed at mooring position $M1_1$ (a,c,e) and $M1_2$ (b,d,f). Teal lines indicate observational data, black lines are the simulations including tides, orange lines refer to the simulations excluding tides. (a), (b) show the full annual cycle for 2014, (c), (d) show a detailed view of the time period February 1-21, (e), (f) are a detailed view of the time period September 1-21.

Both simulated and observed current speed time series show more variability and higher speeds at the upper continental slope, consistent with the presence of the boundary current and the vicinity to the tidally active shelf (Janout and Lenn 2014). Variability and speed are greatest in the fall when sea ice is at a minimum and intermittently in December, which the model captures well (Fig. 5a). During the time periods with high current speed variability, simulations can deviate from the observations over short time scales especially in the energetic environment above the upper slope, but tidal currents are still well-represented (5e). In winter, simulations are very close to the observed current speeds and reproduce variability on sub-daily time scales accurately (Fig. 5c,d).

At the approximately 800 m deep $M1_2$ mooring site, semi-diurnal signals are also reproduced in the simulations without tides (orange line, Fig. 5d,f), suggesting that these signals are predominantly near-inertial oscillations rather than tides. The known proximity of Arctic inertial oscillations and semi-diurnal tides in frequency space complicates their clear separation and introduces large uncertainties in the analysis of tides in the Arctic. This ambiguity must be considered when interpreting, e.g., the distribution of semi-diurnal tidal amplitudes (Fig. 6a,b) and spectra (Fig. 7), particularly for the S_2 component and in regions with weak tidal currents and relatively strong inertial oscillations such as the lower continental slope (Fig. 5d,f). Moreover, calculated velocity anomalies (Fig. 6c) as a proxy for tidal energy include signals from both inertial oscillations and tides, leading to overestimation of tidal strength where inertial oscillations dominate.

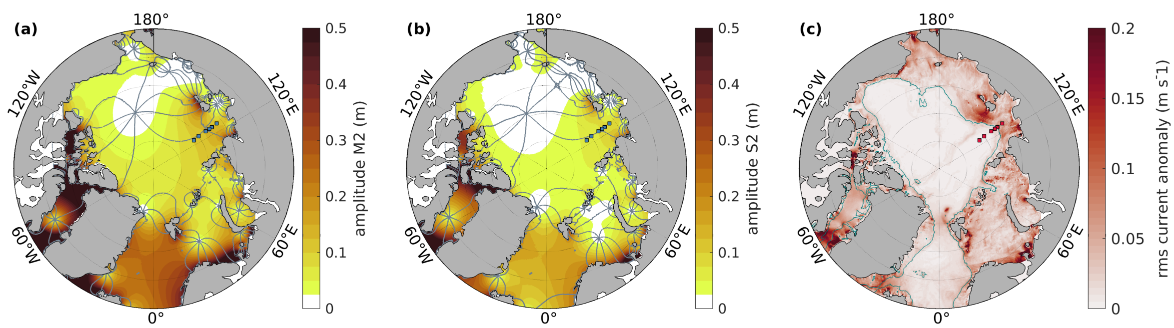

FIG. 6. Amplitude (color coded) and phase (gray lines with 45 degree spacing) for: (a) the principal lunar semi-diurnal M2, and (b) the principal solar S2 constituent. (c) Annual average root mean square current velocity anomaly (m s^{-1}). The teal line in (e) indicates the 500 m isobath, squares indicate the position of the moorings as in Fig. 2.

The regional distribution of tides in the Arctic, as simulated by the presented modeling framework (Fig. 6), accurately reproduces known patterns of tidal activity from observations (Baumann et al. 2020; Hart-Davis et al. 2024), forward barotropic tide models (Erofeeva and Egbert 2020; Howard and Padman 2021) and inverse tidal models (Padman and Erofeeva 2004). Regions of pronounced tidal activity are found east of Svalbard and along the continental coast in the Barents Sea, as well as in Baffin Bay and the Canadian Archipelago. Less intense tidal activity is also evident on the shelf seas around the Arctic, especially in the Laptev Sea (see also Janout and Lenn 2014), and in Fram Strait between Svalbard and Greenland as well as between Iceland and the eastern coast of Greenland. Tidal currents are are negligible in the deep Arctic basins (Fig. 6c).

Tidal currents are strongly influenced by topography and can vary significantly over short distances across the continental slopes. The slopes are also crucial regions for the generation of internal tidal waves and tidal mixing (e.g., Polyakov 1994; Falahat and Nycander 2015; Urbancic et al. 2022; Baumann and Fer 2023). Comparing model output with observations from seven moorings spanning the eastern Eurasian continental slope, ranging from about 50 m to 4000 m depth, allows us to assess the model's performance in a key area of tidal dynamics.

Observations reveal pronounced semidiurnal tidal peaks at all moorings, although their clarity diminishes in the offshore direction (Fig. 7, teal and turquoise lines). Diurnal tidal peaks are only prominent at the upper slope (mooring #1893, $M1_1$, and a faint K_1 peak at $M1_2$). Where distinct tidal peaks occur, the clockwise (CW) component consistently dominates over the counterclockwise (CCW) component, and semidiurnal tides generally exhibit higher energy than diurnal tides. Among the semidiurnal constituents, the M_2 amplitude typically exceeds that of S_2, with exceptions at the offshore moorings $M1_5$ and $M1_6$, where energy in a broad band around S_2 slightly surpasses M_2. This elevated energy in a relatively broad semidiurnal band at the offshore moorings may reflect the influence of energetic near-inertial currents generated during ice-free summers: although barotropic tides are weak at depths greater than 3000 m, short but intense bursts of near-inertial currents, reaching velocities exceeding 0.28 m s^{-1} (data not shown), can significantly contribute to the spectral energy, even when averaged over the two-year observation period.

As expected, the model (Fig. 7, black and gray lines) exhibits a lower noise level than the observations, evident from the lower baseline energy of the gray lines between tidal frequencies. This allows the model to resolve diurnal tidal energy at most mooring locations where the signal is beneath the noise level in the observations. The amplitudes of the modeled and observed spectra align remarkably well at moorings 1893, $M1_1$, and $M1_2$. Further offshore, the simulations match the observed CCW component almost perfectly, but a slight discrepancy is found in the CW component. The model appears to slightly underestimate the energy in the M_2 CW component, showing only faint peaks. However, the broader energy band around the frequency is accurately captured. Overall, the model effectively represents the varying amplitude and composition of tidal energy across the continental slope.

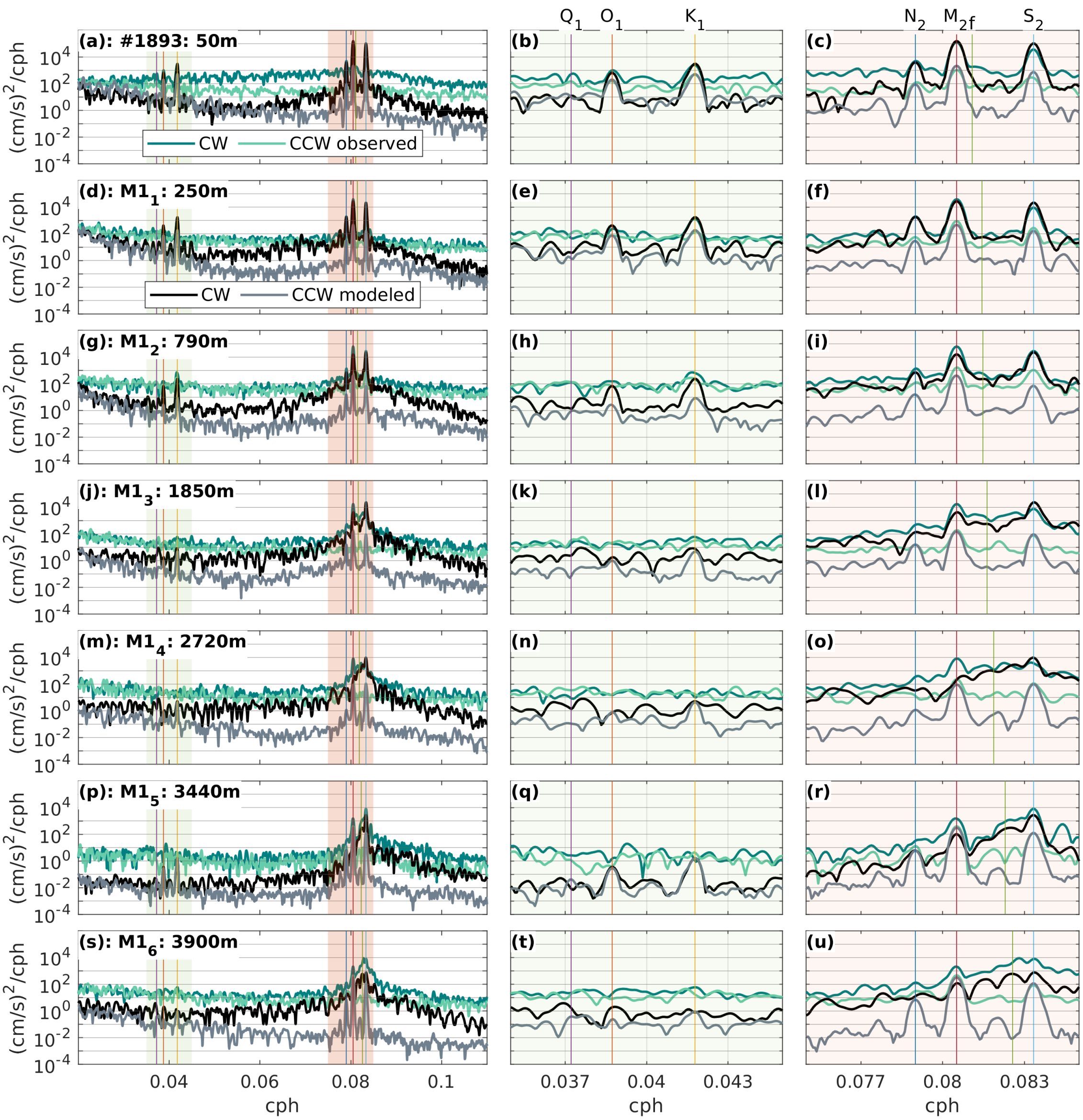

Fig. 7. Left column: Rotary spectra, black and gray colors show the simulated data, teal and turquoise colors the observations from moorings #1893, M1$_1$-M1$_6$. Middle and right columns are zoomed-in on diurnal (green shading) and semidiurnal (red shading) frequency bands, respectively. Colored lines and labels mark the frequencies of the dominant tidal constituents as well as the local inertial frequency (f).

4. The effect of tides on sea ice

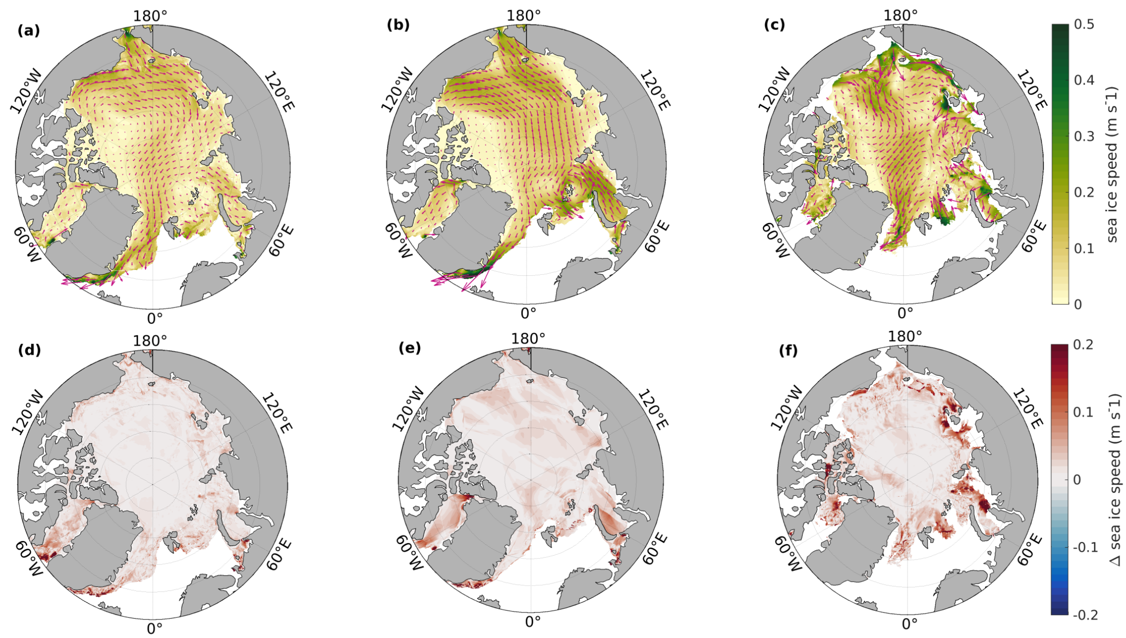

FIG. 8. First row: (a) Annual, (b) winter (January/February), and (c) summer (June /July) mean sea ice velocity for the model run with tides. Second row: Difference in sea ice velocity for the run with and without tides for the same time periods, positive values indicate faster ice drift when tides are included.

The simulated mean ice drift (Fig. 8a) exhibits the known pattern of the anti-cyclonic Beaufort Gyre dominating the circulation in the deep basin. The advection of ice from the Siberian Seas towards Fram Strait (the Transpolar Drift) including the accelerated transport south and towards the east coast of Greenland in Fram Strait is well reproduced. These large scale sea ice circulation pattern are well in line with observed sea ice drift by satellites for the year 2014 (not shown). The simulated ice drift is directed towards the west along the coast of Alaska, crossing the the Chukchi Sea and continuing westwards in the East Siberian Sea. There, the ice partly recirculates in the Beaufort Gyre or is advected into the Transpolar Drift Stream in the Laptev Sea. In winter (Fig. 8b), a northeastward drift in the Kara Sea feeds into a counterclockwise circulation pattern around Franz Josef Land. Strongly elevated ice drift speed is found towards the southern part of the East Greenland Current, flowing south along the eastern coast of Greenland. Intensified northward ice drift near the Alaskan coast and in the Chuckchi Sea north of Bering Strait is present in summer (Fig. 8c), and sea ice velocities are generally high in the marginal ice zone in the Siberian seas, including a westward transport along the East Siberian Sea coast and a northward transport in the Laptev, Kara and Barents Sea. These higher ice speeds in summer are expected, as the sea ice is less compact (reduced sea ice concentration, see Fig. 9c) and thus more susceptible to wind and ocean forcing.

Excluding tides from the simulations (differences shown in Fig. 8d-f) only has a small effect on the ice drift direction and speed in the central Arctic. Tides have a stronger influence on ice advection patterns in Baffin Bay and near the south-eastern Greenland coast, where ice is exported from the Arctic. In summer, tides exert the strongest influence on sea-ice drift in the marginal ice zone throughout the Arctic, likely because the reduced ice concentration allows the ice to remain in a free-drift state that is more susceptible to tidal forcing. Changes in the central basins and in the overall pattern of ice advection, except for in Baffin Bay, are small. Excluding the effect of tidal currents in coupled sea-ice ocean models might hence lead to a misrepresentation of details in ice dynamics in the marginal ice zone and is not an appropriate assumption for regional studies focused on Baffin Bay. However, the pan-Arctic scale ice drift patterns are fairly insensitive to the presence or absence of tides in the simulations.

We see strong regional differences in the effect of tides on sea ice concentration and thickness (Fig. 9). In winter (Fig. 9e,k), tides reduce the sea ice extent in the marginal ice zone in Baffin Bay and Fram Strait, causing the ice edge to be located further north, and increase the open water region around Yermak Plateau. Sea surface temperatures are consistently higher in the Atlantic sector when tides are present (pink line in Fig. 10d, see Fig. 2 for the definition of the region). Especially on the western side of Svalbard, where upward heat flux by enhanced tidal mixing are pronounced (Fer et al. 2020), locally increases sea surface temperature by more than 3°C (June/July average, data not shown), leading to a strongly diminished sea ice concentration in summer (Fig. 9f). Averaged over the Atlantic sector, sea surface temperature is higher by around 0.1°C in the presence of tides (Fig. 10c). However, this region is also a hotspot for ice advection, e.g., southward in the East Greenland Current, and ice dynamics are not only influenced by tidally induced changed in thermodynamics, but also by changes in the surface current patterns.

In contrast, tides slightly increase sea ice at the marginal ice zone in the eastern Barents Sea near Novaya Zemlya, shifting the sea ice edge further south. Winter sea ice thickness is overall reduced in the presence of tides, with a very pronounced reduction in the Canadian Archipelago.

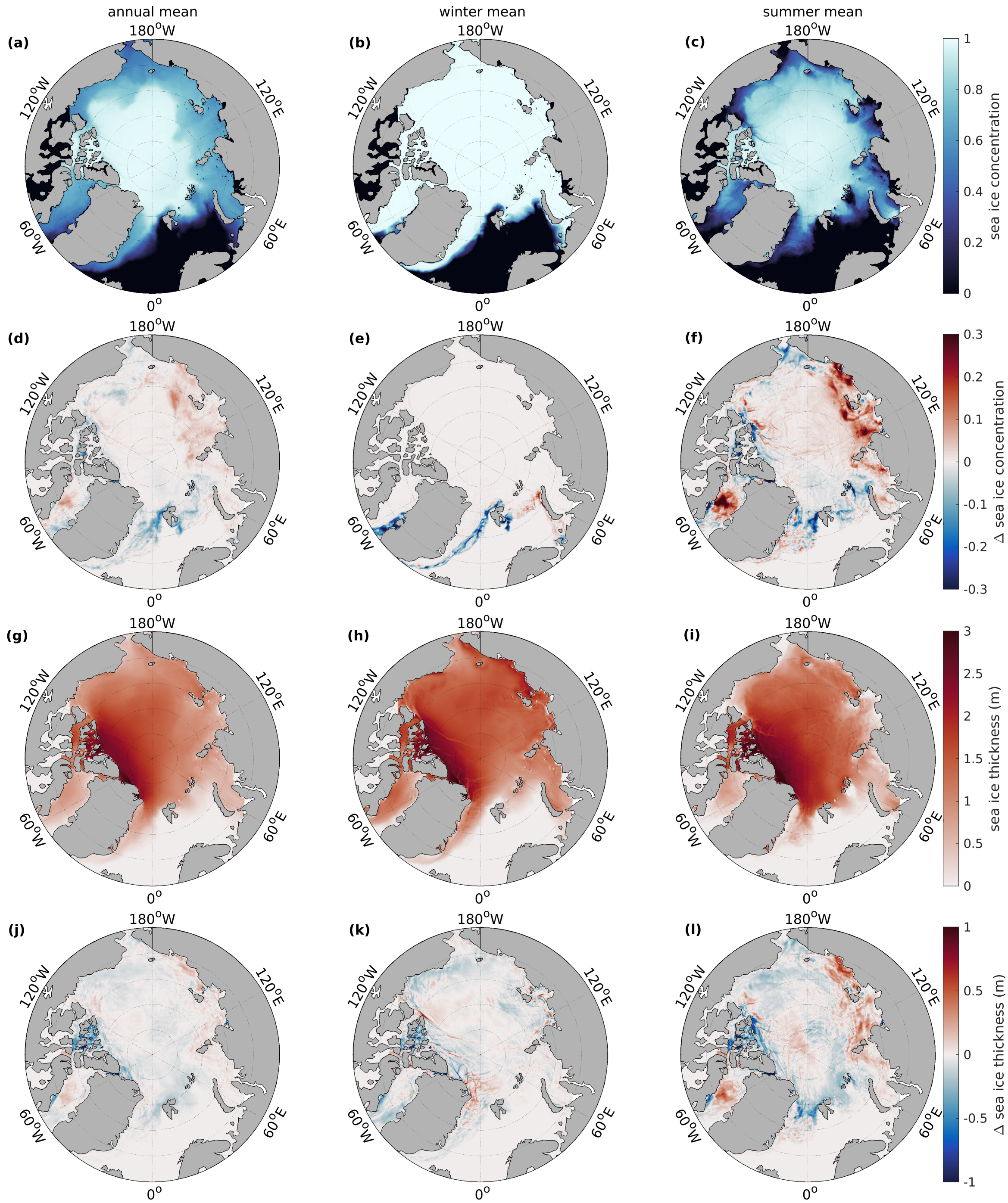

407 FIG. 9. First row: Regional distribution of sea ice concentration for the model run with tides. Second row: Difference in modeled sea ice concentration for the run with and without tides. Third row: Regional distribution of sea ice thickness (m) for the run with tides. Fourth row: Difference in sea ice thickness (m) for the run with and without tides. First column are annual mean values, second column are winter (January/February) mean values, and third column are summer (June/July) mean values. Positive values in (d)-(f), (j)-(l) indicate higher sea ice concentration /thicker sea ice when tides are included in the simulations, respectively.

A slightly increased sea ice thickness is found north of Greenland (Fig. 9k). The northward shift of the marginal ice zone in Baffin Bay and Fram Strait, the increased open waters around Yermak Plateau, as well as the ice thickness reduction in the Canadian Archipelago in winter determine the annually averaged effect of tides in these regions.

In summer (Fig. 9f,l), tides cause an overall strong increase in sea ice concentration in central Baffin Bay. A reduction of sea ice in the northern and southern Baffin Bay points to a change in ice advection patterns by residual tidal currents as described in Kwon and Lee (2016), supported by the simulated high residual ice velocities in Baffin Bay in this study (Fig. 8). However, the regional patterns of tidal influences on sea ice in Baffin Bay are complex, and a detailed analysis lies outside the scope of the presented study.

We also find an increase in summer sea ice concentration in the Laptev and East Siberian Sea, especially on the shelves, which dominates the annual mean signal in this region (Fig. 9d,f). Tidal currents here are stronger than in the central basins (Fig. 6c), especially on the (outer) shelf (Janout and Lenn 2014). Changes in sea ice advection by tides are generally small and confined to the marginal ice zone in this region, pointing to local thermodynamics as a main driver for the increased sea ice concentration (see section 5 below). In contrast, tides reduce sea ice concentration in the Fram Strait and Barents Sea, in line with an increased upward heat flux from the regionally shallower and warmer Atlantic Water layer. Sea ice thickness follows a roughly similar pattern, with an overall thinning near Fram Strait and Bering Strait, and the regions directly downstream, and in the Canadian Arctic Archipelago. Sea ice is thicker in the Laptev Sea and East Siberian Sea near the coast and in central Baffin Bay when tides are included in the simulations.

5. A summer sea ice increase in the Siberian Seas

Integrated over the whole Arctic, tides cause a reduction in sea ice throughout most of the year. When including tides, sea ice area (thick black line in Fig. 10a) is reduced by 0.5-1%, and the average sea ice is 2-6 cm (or 1-5%) thinner, leading to a reduction of the overall sea ice volume by around 2% (thick black line in Fig. 10c). A surprising exception not reported in previous studies is found in June and July, when the sea ice area is around 1.5% *larger* when tides are included in the simulations. Compensated by thinner sea ice, the overall effect on sea ice volume is still negative, but less pronounced (1% instead of 2% reduction) during this time period. The time between July

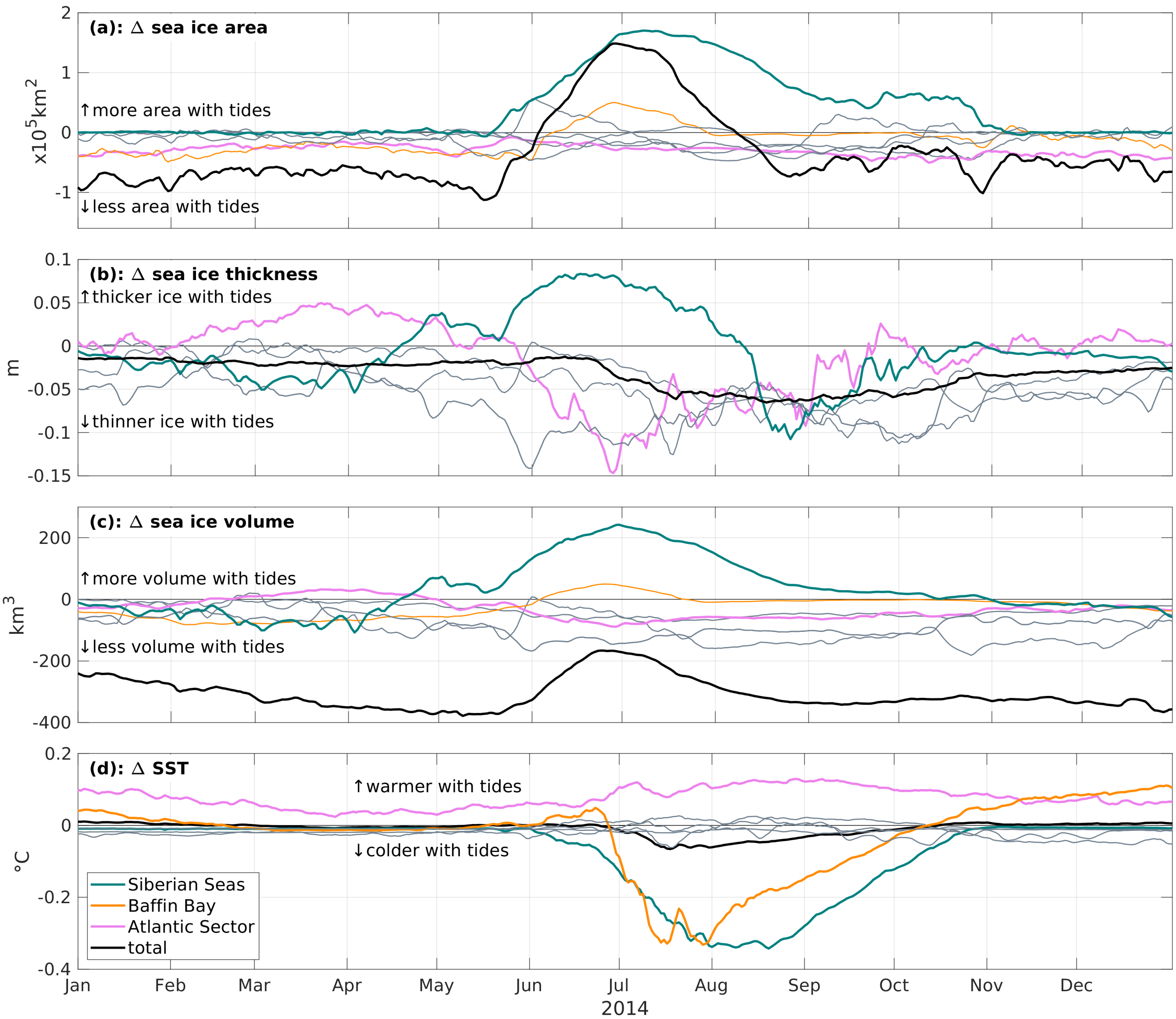

FIG. 10. Difference between modeled daily average (a) sea ice area (km^2), (b) sea ice thickness (m), (c) sea ice volume (km^3), and (d) sea surface temperature (SST, °C) for the runs with and without tides, divided into the contribution by sectors. Siberian Seas is indicated in teal lines, Baffin Bay in orange, the Atlantic Sector in pink, the total seasonal differences are black lines. Changes in the other sectors marked in Fig. 2 are much smaller and only indicated in gray lines for better readability. In (b), sea ice thickness differences in Baffin Bay are occasionally much higher than elsewhere, up to 0.4 m, and therefore not displayed.

and September is also characterized by a slightly lower average sea surface temperature north of 66°N (thick black line in Fig. 10d), indicating that tides might affect sea ice via thermodynamic processes, e.g., via an enhanced downward heat flux in the surface ocean as suggested by the observational findings outlined in section 1.

When dividing the tidal effects on sea ice properties into the regional contributions of the different sectors defined in section 2 (Fig. 2), we find that the summer sea ice area increase in June/July is dominated by changes in sea ice area and volume in the Laptev and East Siberian Seas (teal lines in Fig. 10a,c). This effect is strongest beginning of July, when sea ice volume increase by tides in the Siberian Seas accounts for a difference of 1% in the *pan-Arctic* integrated sea ice volume.

To identify the dominant processes driving the positive regional sea ice anomaly in the presence of tides, we decompose the contributions of individual processes to the temporal evolution of normalized sea ice thickness h_{ice} (m), defined as the sea ice volume in the Siberian sector divided by the total area of the sector as shown in Fig. 2:

$$\partial_t h_{\text{ice}} = G^{\text{adv}} + G^{\text{thermo}}.$$

Here, G^{adv} is the rate of change of h_{ice} due to sea ice transport across the boundary of the Siberian sector, while G^{thermo} denotes the rate of change of h_{ice} driven by thermodynamic processes within the Siberian sector. G^{thermo} can be further decomposed into

$$G^{\text{thermo}} = G^{\text{ocean}} + G^{\text{atmos}} + G^{\text{other}},$$

where G^{ocean} represents the contribution of melting by ocean temperatures above the freezing point. This term is always negative, as sea ice cannot form via this process. The term G^{atmos} represents the rate of change in h_{ice} by atmospheric forcing, including ice formation via the vertical conductive heat flux through sea ice, ice formation in open water and ice melting by warm air temperatures. The contribution from other processes, G^{other}, including flooding events that transform snow into sea ice and sublimation, is found to be negligible. The sea ice budget in our model framework closes to machine precision. For easier interpretation, all the process rates (in m s^{-1}) have been integrated over the respective months to express the absolute change (in m) between the successive monthly model states (Fig. 11a-f). For example, a value of Δh_{ice} =0.4 m for the model run including tides in January (leftmost black diamond in Fig. 11a) indicates that the normalized sea ice thickness in the Siberian sector increased by 0.4 m during that month. This increase is primarily driven by local thermodynamic processes (G^{thermo}, purple bars in Fig. 11a, purple diamonds in Fig. 11d), specifically by new ice formation in either open water or via conductive heat loss from the ocean to the atmosphere (G^{atmos}, blue bars is Fig.11d).

Local thermodynamic processes (purple bars, Fig. 11a) follow the seasonal cycle of ice formation (October to April) and melting (June to August) in the Siberian sector, and typically dominate the total regional change in sea ice (black diamonds, Fig. 11a) – except during the period March to April, when sea ice advection out of the Siberian sector (yellow bars, Fig. 11a) becomes the dominant process. The local thermodynamic processes are primarily governed by atmospheric forcing (blue bars, Fig. 11d). Melting of sea ice by oceanic heat occurs year-round at a small scale, but contributes significantly to the sea ice budget only in summer (June to October, Fig. 11d). The sea ice budgets for the simulations including and excluding tides (Fig. 11a,d and Fig. 11b,e, respectively) are qualitatively similar. The difference between the two simulations (Fig. 11c,f) is about an order of magnitude smaller than the absolute values.

Tides have a pronounced effect on sea ice advection in spring, especially in April, when they reduce sea ice export from the Siberian sector (yellow bars, Fig. 11c), resulting in thicker sea ice in the fully ice covered region. The impact of tide-induced changes in thermodynamics processes on sea ice is generally high in summer (June to August) but small during other months (Fig. 11f). In June, less sea ice is melted by the ocean in the presence of tides (green bars, Fig. 11f), linked to lower sea surface temperatures (Fig.10d) in the region during this period. This combination of advective and local effects leads to the peak positive sea ice volume anomaly in the presence of tides at the end of June (Fig. 10c). In July, lower sea surface temperatures persist, resulting in reduced melting in the presence of tides. However, that effect in compensated by enhanced atmospheric sea ice melting, which becomes more effective with the relatively larger sea ice cover in the presence of tides. Differences in advective patterns play only a minor role during this period. In August, all local processes contribute to increased sea ice melting in the region (Fig. 11f), reducing the differences in sea ice volume and sea surface temperature between the simulations with and without tides (Fig. 10). This trend continues into the fall, albeit less strongly, and, together with ongoing differences in sea ice advection, further reduces the sea ice state differences between the simulations until complete ice cover is reached in early November.

Vertical ocean heat fluxes differ between the simulations due to a combination factors, including prior differences in ocean and sea ice states, shifts in the mesoscale velocity field, and changes

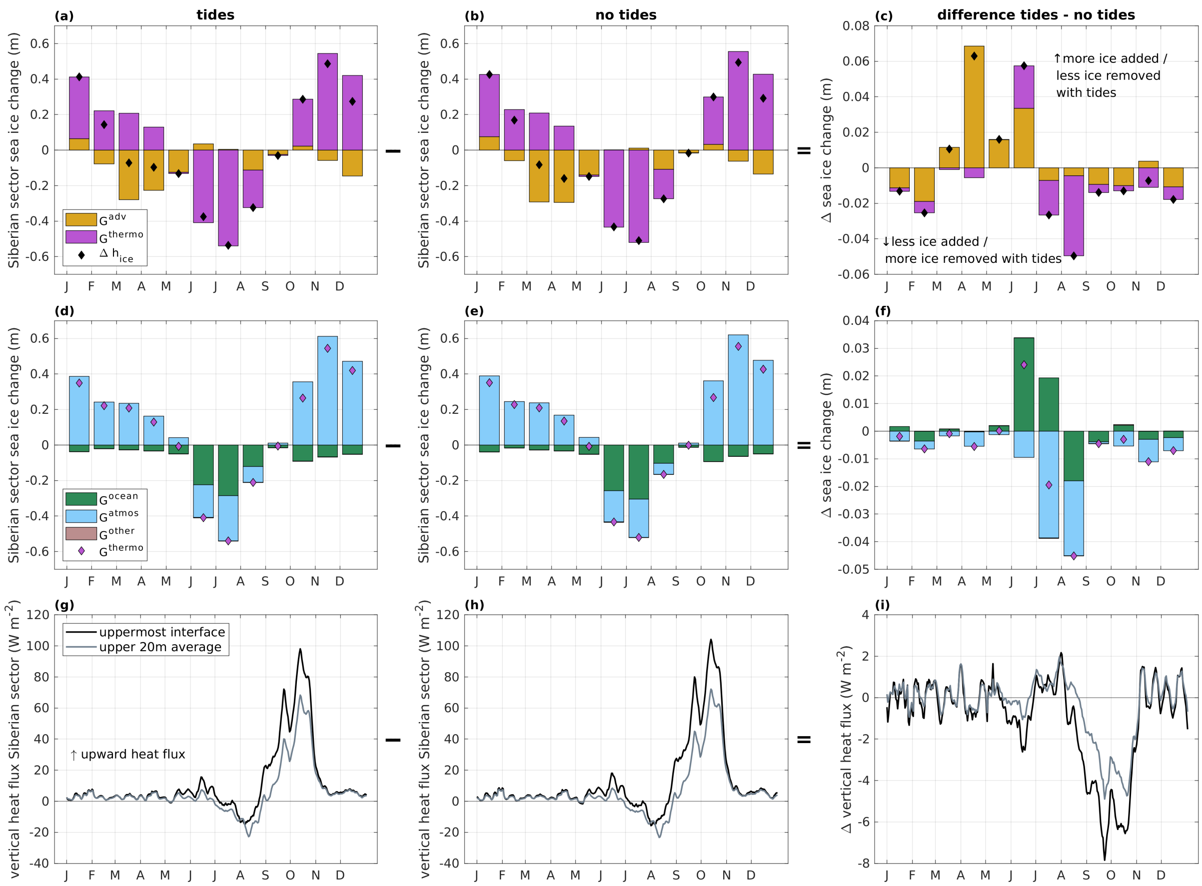

FIG. 11. Partitioning of the monthly change in Siberian sector (see Fig. 2) normalized sea ice thickness (Δh_{ice} in m, black diamonds) due to sea ice advection across the sector boundaries (G^{adv}, yellow bars) and local thermodynamics (G^{thermo}, purple bars) for (a) the simulation including tides, (b) the simulation excluding tides, and (c) the difference between the two simulations, i.e., (a) - (b). Further partitioning of the monthly change in Siberian sector effective sea ice thickness due to local thermodynamics (G^{thermo}, purple diamonds, corresponding to the purple bars in (a)-(c)) into melting by the ocean (G^{ocean}, green bars), sea ice formation of melting by atmospheric forcing (G^{atmos}, blue bars) and other processes (G^{other}, brown bars) for the simulation (d) including tides, (e) excluding tides, and (f) the difference between the two simulations, i.e., (d) - (e). Seasonal variability of the average upper ocean vertical heat fluxes (W m^{-2}) in the Siberian sector for the simulation (g) including and (h) excluding tides, and (i) the difference between both simulations. Positive values in (g), (h) indicate upward heat transport, daily heat flux data are smoothed with a 7-day running mean for better visibility.

in the local dynamics, e.g., increased kinetic energy in the presence of tides. These differences are strongly heterogeneous across small temporal and spatial scales, and the respective drivers of these differences cannot be separated within the model framework. Especially the increasing sea surface temperature difference between the simulations including and excluding tides starting in June (Fig 10d) complicated the interpretation of near-surface vertical heat fluxes.

Between November and May, near-surface vertical heat fluxes are small and generally directed upward in both simulations (Fig. 11g,h), as deep warm water is the only heat source in the absence of solar warming. The presence of tides during this period only leads to minor changes in heat transport, with no consistent directional signal (Fig. 11i). In June, when the sea ice is breaking up, the magnitude of heat fluxes increases, likely to stronger near-surface mixing. Heat fluxes are now a combination of upward heat transport from deep, warm water layers and downward heat transport from solar warming, with upward heat transport still dominating in June (Fig. 11g,h). However, in the presence of tides, this net upward transport is less pronounced (negative values in Fig. 11i). In July and August, the near-surface heat transport switches sign and is directed downward (Fig. 11g,h), the downward transport is slightly weaker in the presence of tides (positive values in Fig. 11i). While this reduced downward heat transport can be partly attributed to the relatively lower sea surface temperatures in the presence of tides (Fig. 10d), it is also consistent with the decrease of sea ice volume difference between the simulations, starting in July (Fig.10c), and the increased melting of sea ice in August (green bar, Fig. 11f). In September and October, heat accumulated in the upper ocean is lost to the atmosphere again, more pronounced in the simulation excluding tides (Fig. 11g-i) with is characterized by warmer upper ocean temperatures throughout the summer. However, differences in local ice melting or formation during this period are considerably smaller compared to the period June to August.

In contrast to other Arctic regions, particularly the Atlantic sector, where tides enhance vertical mixing and transport more heat toward the surface (data not shown), the broad shelves of the Siberian Seas lack a subsurface heat source, such as warm Atlantic or Pacific Water. As a result, no additional heat is available to the surface layer when vertical mixing is increased by tidal processes. More generally, tides can inhibit sea ice melting in summer in regions that meet the following conditions: (a) Tidal velocities are strong enough to significantly alter vertical mixing near the surface; (b) Deep heat reservoirs (e.g., Atlantic or Pacific Water) are either absent (as in shallow shelf seas), located well below the surface, or separated from the surface by strong stratification that limits upward heat transport; and (c) Sufficient open water is present to allow solar heating and establish a surface temperature gradient. Additionally, the impact of this process is modulated by advective patterns, including those induced by tides, which can retain sea ice within regions where tidal processes reduce summer sea ice melting, rather than transporting it into areas with higher melt potential, such as the Atlantic sector. In the Arctic, our results suggest that this combination of factors is most prominently expressed over the wide Siberian shelves, with only minor expressions in smaller regions on other Arctic shelves or in Baffin Bay. In the (seasonally) ice-covered Southern Ocean around Antarctica, tidal velocities are particularly strong in the Weddell Sea (Padman et al. 2018, their Fig. 9). There, deep warm water masses are located at greater depths and are colder than their Arctic counterparts (e.g., Azaneu et al. 2017), making this region a potential candidate for tidal suppression of summer sea ice melt. A similar modeling framework to the one applied in this study could be used to investigate whether tides may also contribute to preserving summer sea ice area around Antarctica by enhancing downward surface heat flux and supporting favorable advective patterns.

6. Discussion

a. Comparison to previous modeling studies

Most results from our state-of-the-art model simulations confirm previous findings, as outlined in detail below. Tides generally decrease sea ice volume in the Arctic, by elevating the turbulent upward heat flux from the warm, deep Atlantic Water layer. This effect is subject to strong regional variability, with hotspots in the Canadian Archipelago, around the Yermak Plateau, and in Fram Strait. Ice advection and redistribution by residual tidal currents are pronounced in Baffin Bay. Increased ice formation in winter due to elevated lead formation in the presence of tides plays a minor role, according to our model results. In contrast to all previous studies, we find an unexpected seasonal increase in Arctic sea ice area caused by tides (Fig. 10a), dominated by processes on the Siberian shelves. These model results, in conjunction with observational data (Fig. 1, section 6b), point to a previously overlooked effect of tides on sea ice: the deceleration of summer ice melt in regions with tidally increased surface downward heat transport.

The first three-dimensional modeling study investigating the effect of tides on sea ice in the Arctic was conducted when computational resources prohibited the explicit inclusion of tides in a pan-Arctic model (Holloway and Proshutinsky 2007). The effect of tides was hence parameterized by adjusting modeled bottom layer turbulent dissipation rates, decaying exponentially with distance from the sea floor to the corresponding depth-integrated values derived from a two-dimensional model (Kowalik and Proshutinsky 1993, 1994). Including this tidal parameterization in the model simulations increased the ventilation of the Atlantic water layer, i.e., elevated upward heat flux, and led to a reduction in sea ice thickness of, on average, 0.6 to 4.5 cm, depending on parameter choices. This reduction roughly matches the range of 2–6 cm (seasonal variability) found in this study. The approach of Holloway and Proshutinsky (2007), however, excludes the contribution to vertical mixing by baroclinic tides, and enhanced mixing in the surface layer.

About a decade later, the most recent model study investigating the role of tides in the Arctic was published (Luneva et al. 2015). The spatial resolution of the model used in Luneva et al. (2015) ranges between 6–15 km, two to five times coarser than in the setup presented here, and includes 50 vertical levels, with the upper 20 being terrain-following. They use a similar background diffusivity of 10^{-6} m^2 s^{-1}, and a second-order turbulence closure instead of KPP. Boundary conditions are taken from a global simulation of a similar model setup excluding tides. In contrast to our study with emphasis on the spatial and seasonal variability of different processes associated with tides, Luneva et al. (2015) focus their analysis on how tides impact Arctic sea ice and water mass transformation trends on a multi-decadal scale.

The model results presented in Luneva et al. (2015) show a reduction in sea ice thickness by 2-5 cm in the presence of tides, in line with our findings, with a regionally strongest decrease in sea ice thickness in the Canadian Archipelago, around Svalbard, and north of Greenland, again in line with our findings (Fig. 9d). In contrast, Luneva et al. (2015) identified the Laptev and East Siberian Seas as sea ice thickness reduction hotspots, while we see an *increase* in sea ice thickness in this region. For sea ice volume, Luneva et al. (2015) report a sea ice volume reduction by on average 3.9%, and up to 6% in September and December when including tides, which is two to three times larger than the sea ice volume reduction we find in our model results.

In addition, there have been regional studies on tidal effects on the sea ice. In the Barents and Kara Sea, Postlethwaite et al. (2011) report a decrease in ice thickness by a few centimeters associated with elevated upward ocean heat fluxes when tides are included, with strong regional gradients even within their smaller model domain, in line with our findings. They also find elevated ice production in winter, as more leads form in the presence of tides, and on average thicker sea ice and more ice volume, a signal that is not dominant in our model results. Kwon and Lee (2016) identified the Canadian Archipelago and Baffin Bay as a region where tides have a strong impact on sea ice conditions. Again, the authors find large regional differences, with a 8.5% increase of sea ice volume in Baffin Bay, resulting from sea ice convergence driven by residual tidal currents, and a 17.8% decrease of sea ice volume in the Canadian Arctic Archipelago, where ice formation in winter is reduced by elevated upward heat flux. These patterns are consistent with our findings (see Fig. 9k for thinner winter sea ice in the Canadian Archipelago, Fig. 9f,l for the convergence of sea ice in the central Baffin Bay).

Our study provides an update on the effects of tides on sea ice, a process that is largely ignored in present day simulations of the Arctic or global climate system. Our findings underscore the potential of synergistic studies and emphasize the need for more observational data, also to refine subgrid-scale parameterizations in models. Combined with advances in numerical schemes and computational capacities that enable finer spatial and temporal resolutions, these refinements will help reduce model bias, progressively enhancing our representation of real-world processes and our understanding of the role of Arctic tides in the coupled Arctic climate system.

b. Observational evidence

The regional distribution of tides, water column stratification and advective processes are reasonably well reproduced in the presented model runs (see section 3). Turbulence and hence vertical heat fluxes, however, are derived from model parameterizations and associated with a larger uncertainty (see below). Direct observations of turbulence in the Arctic Ocean are sparse, and it is challenging to isolate the contribution of tides to vertical mixing in observational data. Nevertheless, existing measurements in various Arctic regions provide evidence supporting the presented model findings.

In the regions around the Yermak Plateau and in Fram Strait, we observed summer near-surface average heat fluxes of -2.1 W m^{-2} (Fig. 1b), occasionally enhanced down to -40 W m^{-2} when tides and sea ice drift are not in phase (see section 1). In the same data set from the MOSAiC campaign in 2020 (Rabe et al. 2022), upward heat fluxes from the Atlantic Water layer were found to be of comparable magnitude, on average 2.1 W m^{-2}, in the absence of strong wind events (Schulz et al. 2024). From a campaign in 2015 in the same region (N-ICE2015, Meyer et al. 2017), we know that in the presence of strong winds, upward heat fluxes from the Atlantic Water layer are much higher, up to 100 W m^{-2}, especially in regions where the Atlantic Water core is very shallow, typically present close to the source of the Atlantic inflow. It is hence realistic that enhanced upward heat flux in the presence of tides dominates over enhanced downward heat flux in summer and that sea ice reduction is particularly pronounced in this region in our model results.

On the continental shelf of the Laptev Sea, Lenn et al. (2011) report periodically elevated mixing by shear production, when the shear vector across the pycnocline, set by the periodic variability of the baroclinic M_2 tide, and the frictional surface stress at the sea ice interface, set by the relative ice drift velocity, are aligned, similar to shear spikes associated with the alignment between the shear vector and wind stress in temperate seas (Burchard and Rippeth 2009). The measurements in Lenn et al. (2011) were obtained in October with a surface layer at freezing point, so we cannot quantify any summer near-surface downward heat fluxes. However, no Atlantic Water is present on the wide shelves of the Laptev or East Siberian Sea as a source of heat, and any elevated downward heat flux in the presence of tides in summer will lower regional sea surface temperature and delay the melting of sea ice on the shelf. In the weakly tidal continental slope region of the Laptev Sea, Schulz et al. (2021) report a downward heat flux of on average -0.3 W m^{-2} over the upper cold halocline layer during September 2018 in open water or close to the marginal ice zone, resulting in a heat flux convergence in the lower halocline. These observational results support the simulated regional reduction of sea surface temperature and the associated increase in sea ice area here.

c. Model uncertainties

Numerical simulations are useful tools for mechanistic investigations of variability, but are subject to uncertainties arising from the initial and open boundary conditions, applied forcing, unconstrained model parameters, and structural model errors (Wunsch et al. 2009; Nguyen et al. 2020, 2021). While efforts were made to reduce some of these uncertainties by incorporating fields (e.g., atmospheric forcing adjustments, open boundary conditions) from a data-constrained state estimate (section 2), biases exist (section 3) that may impact the quantitative assessment presented above.

A key uncertainty is the representation of ocean turbulent mixing and hence vertical heat flux, which plays a pivotal role for sea ice thermodynamic processes. The parameterization for turbulent mixing applied in this study (KPP, Large et al. 1994) is widely used, but known to perform differently across distinct turbulence regimes (Van Roekel et al. 2018). As for most turbulence parameterizations, KPP has been developed for application in the open ocean and introduces biases in the representation of under-ice mixing (e.g., Rosenblum et al. 2021), as energy conversion processes the frictional under-ice boundary layer might differ from the wind-and-wave generated surface mixed layer in the open ocean. Further biases might be introduced by parameterizing convection by brine rejection using convective adjustment (Marotzke 1991), which was tested for surface cooling in the open ocean (Klinger et al. 1996). Furthermore, KPP relies on the assumption of a well-mixed surface mixed layer. In spring and summer, surface buoyancy input from sea ice melting stabilizes the water column and can inhibit the formation of a well-mixed surface layer at least during quiescent ambient conditions (Schulz et al. 2024), rendering the concept of a ”mixed layer” problematic. Unfortunately, there is currently no turbulence parameterization available that is specifically designed and tested for under-ice conditions, primarily due to the lack of observational data. The refinement and validation of turbulence parameterizations using observational data (Souza et al. 2020), e.g., the recent year-long MOSAiC turbulence dataset (Schulz et al. 2022a), could reduce model uncertainties associated with the representation of vertical mixing in under-ice environments and is an important avenue for future work.

An additional model deficiency common to other large-scale ocean and climate models is the inability to skillfully simulate landfast ice (Lemieux et al. 2018), which constitutes an important fraction of Arctic sea ice and typically persists on the Arctic shelves for 7-9 months each year (e.g., Yu et al. 2014). Landfast sea ice decreases atmosphere-ocean exchanges (i.e., of heat, moisture and momentum), reduces mixing in the underlying water column, and alters halocline stability (Itkin et al. 2015). It is observed to extend furthest offshore in the East Siberian, Laptev and Kara Seas (e.g., Yu et al. 2014), which are key areas of strong tidal mixing and delayed summer melting in our model (Fig.9f,l). Efforts to improve the simulation of landfast sea ice include incorporation of a basal drag to enable grounding in regions shallower that a critical depth (Lemieux et al. 2015) and increasing tensile strength to enable arching and maintain the landfast ice cover (Itkin et al. 2015; Lemieux et al. 2016). Lemieux et al. (2018) investigated the impacts of tidal forcing on landfast sea ice including these combined schemes, showing an overall decrease in landfast sea ice extent. This decrease was shown, however, to be largely restricted to areas of strongest tidal forcing (i.e., the

Canadian Arctic Archipelago), with negligible impacts in the eastern Arctic. More recent work has demonstrated that augmenting the basal drag scheme with a lateral drag parameterization further stabilizes landfast sea ice in deeper regions including the Kara Sea, where islands exist to serve as lateral anchor points (Liu et al. 2022). Future work should incorporate this latest parameterization to determine if an improved representation of landfast sea ice qualitatively impacts the results presented here.

Finally, we note that our assessment of tidal impacts is based on simulations of a single year (2014). Determining how tidally-driven mixing mechanisms vary interannually and under ongoing Arctic borealization (Polyakov et al. 2017, 2020a, 2023) should be addressed when longer simulations become available.

7. Summary and Conclusions

In this study, we investigate the effects of tides on Arctic sea ice based on the results of state-of-the-art numerical model simulations, including and excluding tides. Our model results confirm the existence of strong regional differences regarding the dominance of different processes associated with tides, and the overall negative impact on sea ice by elevated upward mixing of heat from warm Atlantic Water. However, this negative effect is less pronounced than previously thought. In contrast to all previous studies, we find an unexpected *increase* in summer sea ice area when tides are included in the simulations, above the Laptev and East Siberian Sea shelves. In this region, sea ice melting is delayed at the start of summer by an increased downward heat transport of surface heat input, and the advection of sea ice into this region is seasonally increased by tides. In contrast to regions further upstream of the boundary current, the warm Atlantic Water core is located relatively deep in the water column, and does not reach the shallow shelf seas.

Our findings underscore the significant regional and seasonal variations in tidal effects on sea ice, posing challenges to assessing the accuracy of representing sea ice conditions in any model that does not incorporate tides, e.g., most ocean and CMIP6-style climate models. Summer sea ice concentration might be underrepresented in some areas, especially above the Siberian continental shelves, and over-represented in others. However, it is improbable that tides represent the primary source of uncertainty in both hindcasts and future projections of Arctic sea ice, given the multitude of contributing factors (Bonan et al. 2021). Notably, the difference resulting from including tides in our simulation is small compared to the large inter-model spread of sea ice area over recent decades in climate models (Notz and SIMIP Community 2020). The latter is partly attributed to the large internal variability in sea ice predictions mostly arising from atmospheric variability (Jahn et al. 2016; Dörr et al. 2021), which in turn affects the oceanic heat import from the Atlantic and subsequent vertical heat flux (Polyakov et al. 2023). This highlights the complex interplay of various factors contributing to the overall uncertainty in Arctic sea ice projections. Nonetheless, while unlikely to be the dominant source of uncertainty in sea ice predictions, particularly in higher resolved coupled sea ice-ocean hindcast models for regions with notable tidal activity, the exclusion of tides can introduce considerable errors in sea ice conditions. These errors may subsequently translate into errors in the prediction of biogeochemical and ecological parameters in coupled model frameworks, e.g., by the misrepresentation of light and nutrient availability due to biases in local sea ice concentration and vertical mixing.

As sea ice is overall declining in the Arctic, longer ice-free seasons will lead to longer periods of strengthened tides (Rotermund et al. 2021). In regions where tides contribute to sea ice loss by upward heat flux, this is a positive feedback mechanism that could accelerate the ongoing sea ice loss associated with anthropogenic climate change. On the other hand, in regions where tidally-induced downward heat flux at the surface dominates over upward heat flux from deeper layers in summer, i.e., where sea ice melting is delayed by tides, sea ice loss trends might be less dramatic, resulting in relatively longer sea ice cover compared to adjacent regions. In combination with elevated surface nutrient (re-)supply induced by stronger vertical mixing (Schulz et al. 2022b), these regions might provide increasingly beneficial conditions for under-ice algae blooms, allowing for longer growing seasons and forming safe havens for the ecosystems endemic to the Arctic. However, the Laptev Sea in particular is also subject to changes by Atlantification (Polyakov et al. 2017), i.e., a progression of conditions rather typical for the Atlantic Ocean along the pathway of the Arctic Boundary Current, entailing competing effects of a shallower Atlantic Water layer, enhanced upward vertical heat flux and hence sea ice reduction. Future monitoring of both oceanographic and sea ice conditions as well as advances in numerical modeling are needed to disentangle distinct drivers of changing conditions and accurately predict trends for Arctic sea ice.

Acknowledgments. Observational data displayed in the introduction were produced as part of the international Multidisciplinary drifting Observatory for the Study of the Arctic Climate (MOSAiC) project with the tag MOSAiC20192020 and the Project_ID: AWI_PS122_00. We thank all persons involved in the expedition of the Research Vessel *Polarstern* (Knust 2017) during MOSAiC in 2019-2020 as listed in the MOSAiC extended acknowledgment (Nixdorf et al. 2021). Hydrographic data used for model validation were obtained under the framework of the NABOS project with support from NSF (Grants AON-1203473 and AON-1947162). Contour plots were produced using the cmocean colormaps (Thyng et al. 2016), maps were produced using the M_Map Matlab toolbox (Pawlowicz 2000). KS, ATN and HP received support from the National Science Foundation grant NSF-OCE-2401413, ATN and KS received further support via the NSF-AccelNet-2020387 grant, ATN also received funding from grant NSF-OPP-1936579. IF and TMB received support from the Research Council of Norway (AROMA, Arctic Ocean mixing processes and vertical fluxes of energy and matter, Grant 294396). MM and GS received funding from the European Union's Horizon 2020 research and innovation program under grant agreement No 101003826 via project CRiceS.

Data availability statement. Model results used in the study are available at Nguyen (2022). Observational data shown in this study are publicly available at Schulz et al. (2023b) for the MOSAiC microstructure profiles; Baumann et al. (2021) for the MOSAiC 75 kHz ADCP and position data; Muilwijk and Polyakov (2022) for the Arctic Ocean hydrographic profiles, and Polyakov (2016) for the NABOS mooring array.

References

Adcroft, A., J.-M. Campin, C. Hill, and J. Marshall, 2004: Implementation of an atmosphere–ocean general circulation model on the expanded spherical cube. *Monthly Weather Review*, **132 (12)**, 2845–2863, https://doi.org/10.1175/MWR2823.1.

Adcroft, A., and Coauthors, 2018: *MITgcm User Manual*. URL http://hdl.handle.net/1721.1/117188.

Antonov, J. I., and Coauthors, 2010: *World Ocean Atlas 2005 Volume 2: Salinity*. Levitus (2010), URL http://www.nodc.noaa.gov/OC5/indprod.html.

Arbic, B., and Coauthors, 2018: A primer on global internal tide and internal gravity wave continuum modeling in HYCOM and MITgcm. *New Frontiers in Operational Oceanography*,

E. Chassignet, A. Pascual, J. Tintoré, and J. Verron, Eds., GODAE OceanView, CreateSpace Independent Publishing Platform, 307–392, https://doi.org/10.17125/gov2018.ch13.

Azaneu, M., K. J. Heywood, B. Y. Queste, and A. F. Thompson, 2017: Variability of the Antarctic slope current system in the Northwestern Weddell sea. *Journal of Physical Oceanography*, **47 (12)**, 2977–2997, https://doi.org/https://doi.org/10.1175/JPO-D-17-0030.1.

Baker, M. A., and C. H. Gibson, 1987: Sampling turbulence in the stratified ocean: Statistical consequences of strong intermittency. *Journal of Physical Oceanography*, **17 (10)**, 1817–1836, https://doi.org/10.1175/1520-0485(1987)017⟨1817:STITSO⟩2.0.CO;2.

Baumann, T., and Coauthors, 2021: Under-ice current measurements during MOSAiC from a 75 kHz acoustic Doppler profiler. PANGAEA, https://doi.org/10.1594/PANGAEA.934792.

Baumann, T. M., and I. Fer, 2023: Trapped tidal currents generate freely propagating internal waves at the Arctic continental slope. *Scientific Reports*, **13 (1)**, 14 816, https://doi.org/10.1038/s41598-023-41870-3.

Baumann, T. M., I. V. Polyakov, L. Padman, S. Danielson, I. Fer, M. Janout, W. Williams, and A. V. Pnyushkov, 2020: Arctic tidal current atlas. *Scientific data*, **7 (1)**, 275, https://doi.org/10.1038/s41597-020-00578-z.

Baumann, T. M., I. V. Polyakov, A. V. Pnyushkov, R. Rember, V. V. Ivanov, M. B. Alkire, I. Goszczko, and E. C. Carmack, 2018: On the seasonal cycles observed at the continental slope of the Eastern Eurasian Basin of the Arctic Ocean. *Journal of Physical Oceanography*, **48 (7)**, 1451–1470, https://doi.org/10.1175/JPO-D-17-0163.1.

Bonan, D. B., F. Lehner, and M. M. Holland, 2021: Partitioning uncertainty in projections of Arctic sea ice. *Environmental Research Letters*, **16 (4)**, 044 002, https://doi.org/10.1088/1748-9326/abe0ec.

Bouffard, D., and L. Boegman, 2013: A diapycnal diffusivity model for stratified environmental flows. *Dynamics of Atmospheres and Oceans*, **61**, 14–34, https://doi.org/10.1016/j.dynatmoce.2013.02.002.

Burchard, H., and T. P. Rippeth, 2009: Generation of bulk shear spikes in shallow stratified tidal seas. *Journal of Physical Oceanography*, **39 (4)**, 969–985, https://doi.org/10.1175/2008JPO4074.1.

Campin, J.-M., A. Adcroft, C. Hill, and J. Marshall, 2004: Conservation of properties in a free-surface model. *Ocean Modelling*, **6 (3)**, 221–244, https://doi.org/10.1016/S1463-5003(03)00009-X.

Dörr, J., M. Årthun, T. Eldevik, and E. Madonna, 2021: Mechanisms of regional winter sea-ice variability in a warming arctic. *Journal of Climate*, **34 (21)**, 8635–8653, https://doi.org/10.1175/JCLI-D-21-0149.1.

Egbert, G. D., and S. Y. Erofeeva, 2002: Efficient inverse modeling of barotropic ocean tides. *Journal of Atmospheric and Oceanic technology*, **19 (2)**, 183–204, https://doi.org/10.1175/1520-0426(2002)019⟨0183:EIMOBO⟩2.0.CO;2.

Erofeeva, S., and G. Egbert, 2020: Arc5km2018: Arctic Ocean Inverse Tide Model on a 5 kilometer grid, 2018. Dataset. https://doi.org/10.18739/A21R6N14K.

Falahat, S., and J. Nycander, 2015: On the generation of bottom-trapped internal tides. *Journal of Physical Oceanography*, **45 (2)**, 526–545, https://doi.org/10.1175/JPO-D-14-0081.1.

Fer, I., 2009: Weak vertical diffusion allows maintenance of cold halocline in the central Arctic. *Atmospheric and Oceanic Science Letters*, **2 (3)**, 148–152, https://doi.org/10.1080/16742834.2009.11446789.

Fer, I., Z. Koenig, I. E. Kozlov, M. Ostrowski, T. P. Rippeth, L. Padman, A. Bosse, and E. Kolås, 2020: Tidally Forced Lee Waves Drive Turbulent Mixing Along the Arctic Ocean Margins. *Geophysical Research Letters*, **47 (16)**, e2020GL088 083, https://doi.org/10.1029/2020GL088083.

Flexas, M. M., A. F. Thompson, H. S. Torres, P. Klein, J. T. Farrar, H. Zhang, and D. Menemenlis, 2019: Global estimates of the energy transfer from the wind to the ocean, with emphasis on near-inertial oscillations. *Journal of Geophysical Research: Oceans*, **124 (8)**, 5723–5746, https://doi.org/10.1029/2018JC014453.

Grabs, W., F. Portmann, and T. de Couet, 2000: *Discharge Observation Networks in Arctic Regions: Computation of the River Runoff into the Arctic Ocean, Its Seasonality and Variability*, 249–267. Springer Netherlands, Dordrecht, https://doi.org/10.1007/978-94-011-4132-1_11, URL 10.1007/978-94-011-4132-1_11.

Hannah, C. G., F. Dupont, and M. Dunphy, 2009: Polynyas and tidal currents in the canadian arctic archipelago. *Arctic*, 83–95, https://doi.org/10.14430/arctic115.

Hart-Davis, M. G., S. L. Howard, R. D. Ray, O. B. Andersen, L. Padman, F. Nilsen, and D. Dettmering, 2024: ArcTiCA: Arctic tidal constituents atlas. *Scientific Data*, **11 (1)**, 167, https://doi.org/10.1038/s41597-024-03012-w.

Heimbach, P., D. Menemenlis, M. Losch, J.-M. Campin, and C. Hill, 2010: On the formulation of sea-ice models. Part 2: Lessons from multi-year adjoint sea-ice export sensitivities through the Canadian Arctic Archipelago. *Ocean Modelling*, **33 (1-2)**, 145–158, https://doi.org/10.1016/j.ocemod.2010.02.002.

Heuzé, C., H. Zanowski, S. Karam, and M. Muilwijk, 2023: The deep Arctic Ocean and Fram Strait in CMIP6 models. *Journal of Climate*, **36 (8)**, 2551–2584, https://doi.org/10.1175/JCLI-D-22-0194.1.

Holloway, G., and A. Proshutinsky, 2007: Role of tides in Arctic ocean/ice climate. *Journal of Geophysical Research: Oceans*, **112 (C4)**, https://doi.org/10.1029/2006JC003643.

Howard, S., and L. Padman, 2021: Arc2kmTM: Arctic 2 kilometer tide model, 2021. Arctic Data Center, https://doi.org/10.18739/A2PV6B79W.

Itkin, P., M. Losch, and R. Gerdes, 2015: Landfast ice affects the stability of the Arctic halocline: Evidence from a numerical model. *Journal of Geophysical Research: Oceans*, **120 (4)**, 2622–2635, https://doi.org/10.1002/2014JC010353.

Jahn, A., J. E. Kay, M. M. Holland, and D. M. Hall, 2016: How predictable is the timing of a summer ice-free arctic? *Geophysical Research Letters*, **43 (17)**, 9113–9120, https://doi.org/10.1002/2016GL070067.

Janout, M. A., and Y.-D. Lenn, 2014: Semidiurnal tides on the Laptev Sea shelf with implications for shear and vertical mixing. *Journal of Physical Oceanography*, **44 (1)**, 202–219, https://doi.org/10.1175/JPO-D-12-0240.1.

Klinger, B. A., J. Marshall, and U. Send, 1996: Representation of convective plumes by vertical adjustment. *Journal of Geophysical Research: Oceans*, **101 (C8)**, 18 175–18 182, https://doi.org/10.1029/96JC00861.

Knust, R., 2017: Polar research and supply vessel POLARSTERN operated by the Alfred-Wegener-Institute. *Journal of Large-Scale Research Facilities*, **3**, A119, https://doi.org/10.17815/jlsrf-3-163.

Kobayashi, S., and Coauthors, 2015: The JRA-55 reanalysis: General specifications and basic characteristics. *Journal of the Meteorological Society of Japan. Ser. II*, **93 (1)**, 5–48, https://doi.org/10.2151/jmsj.2015-001.

Kowalik, Z., and A. Y. Proshutinsky, 1993: Diurnal tides in the Arctic Ocean. *Journal of Geophysical Research: Oceans*, **98 (C9)**, 16 449–16 468, https://doi.org/10.1029/93JC01363.

Kowalik, Z., and A. Y. Proshutinsky, 1994: The Arctic Ocean Tides. *Washington DC American Geophysical Union Geophysical Monograph Series*, **85**, 137–158, https://doi.org/10.1029/GM085p0137.

Kwon, M. O., and H. J. Lee, 2016: The effect of tides on the volume of sea ice in the Arctic Ocean. *Ocean Science Journal*, **51**, 183–194, https://doi.org/10.1007/s12601-016-0016-x.

Large, W. G., J. C. McWilliams, and S. C. Doney, 1994: Oceanic vertical mixing: a review and a model with nonlocal boundary layer parameterization. *Rev. Geophys.*, **32**, 363–403, https://doi.org/10.1029/94RG01872.

Large, W. G., and S. G. Yeager, 2008: The global climatology of an interannually varying air–sea flux data set. *Clim. Dyn.*, **33 (2–3)**, 341–364.

Lemieux, J.-F., F. Dupont, P. Blain, F. Roy, G. C. Smith, and G. M. Flato, 2016: Improving the simulation of landfast ice by combining tensile strength and a parameterization for grounded ridges. *Journal of Geophysical Research: Oceans*, **121 (10)**, 7354–7368, https://doi.org/10.1002/2016JC012006.

Lemieux, J.-F., J. Lei, F. Dupont, F. Roy, M. Losch, C. Lique, and F. Laliberté, 2018: The impact of tides on simulated landfast ice in a Pan-Arctic ice-ocean model. *Journal of Geophysical Research: Oceans*, **123 (11)**, 7747–7762, https://doi.org/10.1029/2018JC014080.

Lemieux, J.-F., L. B. Tremblay, F. Dupont, M. Plante, G. C. Smith, and D. Dumont, 2015: A basal stress parameterization for modeling landfast ice. *Journal of Geophysical Research: Oceans*, **120 (4)**, 3157–3173, https://doi.org/10.1002/2014JC010678.

Lenn, Y.-D., T. P. Rippeth, C. P. Old, S. Bacon, I. Polyakov, V. Ivanov, and J. Hölemann, 2011: Intermittent intense turbulent mixing under ice in the laptev sea continental shelf. *Journal of Physical Oceanography*, **41 (3)**, 531–547, https://doi.org/10.1175/2010JPO4425.1.

Levitus, S. N. A. N. . U. G. P. O. W. D., Ed., 2010: *World Ocean Atlas 2009*. NOAA Atlas NESDIS 68, U.S. Government Printing Office, Washington, D.C.

Liu, Y., M. Losch, N. Hutter, and L. Mu, 2022: A new parameterization of coastal drag to simulate landfast ice in deep marginal seas in the arctic. *Journal of Geophysical Research: Oceans*, **127 (6)**, e2022JC018 413, https://doi.org/10.1029/2022JC018413.

Locarnini, R. A., and Coauthors, 2010: *World Ocean Atlas 2005 Volume 1: Temperature*. Levitus (2010).

Losch, M., and S. Danilov, 2012: On solving the momentum equations of dynamic sea ice models with implicit solvers and the elastic–viscous–plastic technique. *Ocean Modelling*, **41**, 42–52, https://doi.org/10.1016/j.ocemod.2011.10.002.

Luneva, M. V., Y. Aksenov, J. D. Harle, and J. T. Holt, 2015: The effects of tides on the water mass mixing and sea ice in the Arctic Ocean. *Journal of Geophysical Research: Oceans*, **120 (10)**, 6669–6699, https://doi.org/10.1002/2014JC010310.

Marotzke, J., 1991: Influence of convective adjustment on the stability of the thermohaline circulation. *Journal of Physical Oceanography*, **21 (6)**, 903–907, https://doi.org/10.1175/1520-0485(1991)021⟨0903:IOCAOT⟩2.0.CO;2.

Marshall, J., A. Adcroft, C. Hill, L. Perelman, and C. Heisey, 1997: A finite-volume, incompressible navier stokes model for studies of the ocean on parallel computers. *Journal of Geophysical Research: Oceans*, **102 (C3)**, 5753–5766, https://doi.org/10.1029/96JC02775.

McDougall, T. J., and P. M. Barker, 2011: *Getting started with TEOS-10 and the Gibbs Seawater (GSW) Oceanographic Toolbox*. SCOR/IAPSO, 28 pp., URL www.TEOS-10.org.

Meyer, A., I. Fer, A. Sundfjord, and A. K. Peterson, 2017: Mixing rates and vertical heat fluxes north of svalbard from arctic winter to spring. *Journal of Geophysical Research: Oceans*, **122 (6)**, 4569–4586, https://doi.org/10.1002/2016JC012441.

Muilwijk, M., and I. Polyakov, 2022: Vertical profiles of temperature and salinity in the central arctic ocean from observations and 13 cmip6 models - 1970-2017. Arctic Data Center., URL https://arcticdata.io/catalog/view/doi:10.18739/A20P0WS23, https://doi.org/https://doi:10.18739/A20P0WS23.

Müller, M., H. Haak, J. H. Jungclaus, J. Sündermann, and M. Thomas, 2010: The effect of ocean tides on a climate model simulation. *Ocean Modelling*, **35 (4)**, 304–313, https://doi.org/10.1016/j.ocemod.2010.09.001.

Nansen, F., and O. N. Sverdrup, 1898: *Farthest North: Being the Record of a Voyage of Exploration of the Ship" Fram" 1893-96, and of a Fifteen Months' Sleigh Journey by Dr. Nansen and Lieut. Johansen*. Harper & Brothers Publishers.

Nguyen, A., 2022: Arctic Ocean 3.5 kilometer model monthly mean outputs for 2014 and configuration for rerunning model with and without tides. Arctic Data Center, URL doi:10.18739/A26T0GX63.

Nguyen, A., P. Heimbach, V. Garg, V. O. na, C. Lee, and L. Rainville, 2020: Impact of synthetic Arctic Argo-type floats in a coupled ocean-sea ice state estimation framework. *J. Atmos. Ocean Technol.*, **37 (8)**, 1477–1495, https://doi.org/10.1175/JTECH-D-19-0159.1.

Nguyen, A., D. Menemenlis, and R. Kwok, 2009: Improved modeling of the Arctic halocline with a subgrid-scale brine rejection parameterization. *Journal of Geophysical Research: Oceans*, **114 (C11)**, https://doi.org/10.1029/2008JC005121.

Nguyen, A., D. Menemenlis, and R. Kwok, 2011: Arctic ice-ocean simulations with optimized model parameters: approach and assessment. *J. Geophys. Res.*, **116 (C4)**, C04 025, https://doi.org/10.1029/2010JC006573.

Nguyen, A., H. Pillar, V. Ocaña, A. Bigdeli, T. Smith, and P. Heimbach, 2021: The Arctic Subpolar Gyre sTate Estimate: Description and Assessment of a Data-Constrained, Dynamically Consistent Ocean-Sea Ice Estimate for 2002–2017. *Journal of Advances in Modeling Earth Systems*, **13 (5)**, e2020MS002 398, https://doi.org/10.1029/2020MS002398.

Nikurashin, M., and R. Ferrari, 2013: Overturning circulation driven by breaking internal waves in the deep ocean. *Geophys. Res. Lett.*, **40**, 3133–3137, https://doi.org/10.1002/grl.50542.

Nixdorf, U., and Coauthors, 2021: Mosaic extended acknowledgement. Zenodo, https://doi.org/10.5281/zenodo.5541624.

Notz, D., and SIMIP Community, 2020: Arctic sea ice in CMIP6. *Geophysical Research Letters*, **47**, e2019GL086 749, https://doi.org/10.1029/2019GL086749.

Padman, L., and T. M. Dillon, 1991: Turbulent mixing near the Yermak Plateau during the coordinated Eastern Arctic Experiment. *Journal of Geophysical Research: Oceans*, **96 (C3)**, 4769–4782, https://doi.org/10.1029/90JC02260.

Padman, L., and S. Erofeeva, 2004: A barotropic inverse tidal model for the Arctic Ocean. *Geophysical Research Letters*, **31 (2)**, https://doi.org/10.1029/2003GL019003.

Padman, L., A. J. Plueddemann, R. D. Muench, and R. Pinkel, 1992: Diurnal tides near the Yermak Plateau. *Journal of Geophysical Research: Oceans*, **97 (C8)**, 12 639–12 652, https://doi.org/10.1029/92JC01097.

Padman, L., M. R. Siegfried, and H. A. Fricker, 2018: Ocean tide influences on the Antarctic and Greenland ice sheets. *Reviews of Geophysics*, **56 (1)**, 142–184, https://doi.org/10.1002/2016RG000546.

Pawlowicz, R., 2000: M_Map: A mapping package for Matlab. *University of British Columbia Earth and Ocean Sciences.[Online]. Available: http://www. eos. ubc. ca/rich/map. html.*

Polyakov, I., 1994: Maintenance of the Arctic Ocean large-scale baroclinic structure by the M2 tide. *Polar Research*, **13 (2)**, 219–232, https://doi.org/10.1111/j.1751-8369.1994.tb00451.x.

Polyakov, I. V., 2016: NABOS II - ADCP Water Current Data 2013 - 2015. https://doi.org/10.18739/A28G8FJ3H.

Polyakov, I. V., R. B. Ingvaldsen, A. V. Pnyushkov, U. S. Bhatt, J. A. Francis, M. Janout, R. Kwok, and Ø. Skagseth, 2023: Fluctuating atlantic inflows modulate arctic atlantification. *Science*, **381 (6661)**, 972–979, https://doi.org/10.1126/science.adh5158.

Polyakov, I. V., and Coauthors, 2017: Greater role for Atlantic inflows on sea-ice loss in the eurasian basin of the arctic ocean. *Science*, **356 (6335)**, 285–291, https://doi.org/10.1126/science.aai8204.

Polyakov, I. V., and Coauthors, 2020a: Borealization of the Arctic Ocean in response to anomalous advection from sub-Arctic seas. *Frontiers in Marine Science*, **7**, 491, https://doi.org/10.3389/fmars.2020.00491.

Polyakov, I. V., and Coauthors, 2020b: Intensification of near-surface currents and shear in the Eastern Arctic Ocean. *Geophysical Research Letters*, **47 (16)**, e2020GL089 469, https://doi.org/10.1029/2020GL089469.

Polyakov, I. V., and Coauthors, 2025: Atlantification advances into the Amerasian Basin of the Arctic Ocean. *Science Advances*, **11 (8)**, eadq7580, https://doi.org/10.1126/sciadv.adq7580.

Ponte, R., A. Chaudhuri, and S. V. Vinogradov, 2015: Long-period tides in an atmospheric driven, stratified ocean. *J. Phys. Oceanogr.*, **45**, 1917–1928, https://doi.org/10.1175/JPO-D-15-0006.1.

Ponte, R., and S. V. Vinogradov, 2007: Effects of stratification on the large-scale ocean response to barometric pressure. *J. Phys. Oceanogr.*, **37**, 245–258, https://doi.org/10.1175/JPO3010.1.

Postlethwaite, C., M. Maqueda, V. Le Fouest, G. Tattersall, J. Holt, and A. Willmott, 2011: The effect of tides on dense water formation in arctic shelf seas. *Ocean Science*, **7 (2)**, 203–217, https://doi.org/10.5194/os-7-203-2011.

Rabe, B., and Coauthors, 2022: Overview of the MOSAiC expedition: Physical oceanography. *Elementa: Science of the Anthropocene*, **10 (1)**, https://doi.org/10.1525/elementa.2021.00062.

Rippeth, T. P., B. J. Lincoln, Y.-D. Lenn, J. M. Green, A. Sundfjord, and S. Bacon, 2015: Tide-mediated warming of Arctic halocline by Atlantic heat fluxes over rough topography. *Nature Geoscience*, **8 (3)**, 191, https://doi.org/10.1038/ngeo2350.

Rosenblum, E., R. Fajber, J. Stroeve, S. Gille, L. Tremblay, and E. Carmack, 2021: Surface salinity under transitioning ice cover in the Canada Basin: Climate model biases linked to vertical distribution of fresh water. *Geophysical Research Letters*, **48 (21)**, e2021GL094 739, https://doi.org/10.1029/2021GL094739.

Rotermund, L. M., W. J. Williams, J. M. Klymak, Y. Wu, R. K. Scharien, and C. Haas, 2021: The effect of sea ice on tidal propagation in the Kitikmeot Sea, Canadian Arctic Archipelago. *Journal of Geophysical Research: Oceans*, **126 (5)**, e2020JC016 786, https://doi.org/10.1029/2020JC016786.

Schulz, K., D. Kadko, V. Mohrholz, M. Stephens, and I. Fer, 2023a: Winter vertical diffusion rates in the Arctic Ocean, estimated from 7be measurements and dissipation rate profiles. *Journal of Geophysical Research: Oceans*, e2022JC019197, https://doi.org/10.1029/2022JC019197.

Schulz, K., V. Mohrholz, I. Fer, M. Janout, M. Hoppmann, J. Schaffer, and Z. Koenig, 2022a: A full year of turbulence measurements from a drift campaign in the Arctic Ocean 2019—2020. *Scientific Data*, **9 (472)**, https://doi.org/10.1038/s41597-022-01574-1.

Schulz, K., and Coauthors, 2021: On the along-slope heat loss of the Boundary Current in the Eastern Arctic Ocean. *Journal of Geophysical Research: Oceans*, **126 (2)**, e2020JC016 375, https://doi.org/10.1029/2020JC016375.

Schulz, K., and Coauthors, 2022b: Increasing nutrient fluxes and mixing regime changes in the eastern Arctic Ocean. *Geophysical Research Letters*, e2021GL096152, https://doi.org/10.1029/2021GL096152.

Schulz, K., and Coauthors, 2023b: Turbulent microstructure profile (MSS) measurements from the MOSAiC drift, Arctic Ocean, version 2. PANGAEA, https://doi.org/https://doi.pangaea.de/10.1594/PANGAEA.961798.

Schulz, K., and Coauthors, 2024: The Eurasian Arctic Ocean along the MOSAiC drift in 2019–2020: An interdisciplinary perspective on physical properties and processes. *Elementa: Science of the Anthropocene*, **12 (1)**, https://doi.org/10.1525/elementa.2023.00114.

Semtner, A., 1976: A model for the thermodynamic growth of sea ice in numerical investigations of climate. *Journal of Physical Oceanography*, **6 (3)**, 379–389, https://doi.org/10.1175/1520-0485(1976)006⟨0379:AMFTTG⟩2.0.CO;2.

Song, P., D. Sidorenko, P. Scholz, M. Thomas, and G. Lohmann, 2023: The tidal effects in the Finite-volumE Sea ice–Ocean Model (FESOM2. 1): a comparison between parameterised tidal mixing and explicit tidal forcing. *Geoscientific Model Development*, **16 (1)**, 383–405, https://doi.org/10.5194/gmd-16-383-2023.

Souza, A. N., and Coauthors, 2020: Uncertainty quantification of ocean parameterizations: Application to the K-profile-parameterization for penetrative convection. *Journal of Advances in Modeling Earth Systems*, **12 (12)**, e2020MS002 108, https://doi.org/10.1029/2020MS002108.

Steele, M., W. Ermold, and J. Zhang, 2011: Modeling the formation and fate of the near-surface temperature maximum in the Canadian Basin of the Arctic Ocean. *Journal of Geophysical Research: Oceans*, **116 (C11)**, https://doi.org/10.1029/2010JC006803.

Stewart, K., and Coauthors, 2020: Jra55-do-based repeat year forcing datasets for driving ocean–sea-ice models. *Ocean Modelling*, **147**, 101 557, https://doi.org/10.1016/j.ocemod.2019.101557.

Thyng, K. M., C. A. Greene, R. D. Hetland, H. M. Zimmerle, and S. F. DiMarco, 2016: True colors of oceanography: Guidelines for effective and accurate colormap selection. *Oceanography*, **29 (3)**, 9–13, https://doi.org/https://www.jstor.org/stable/24862699.

Urbancic, G. H., K. G. Lamb, I. Fer, and L. Padman, 2022: The generation of linear and nonlinear internal waves forced by subinertial tides over the Yermak Plateau, Arctic Ocean. *Journal of Physical Oceanography*, **52 (9)**, 2183–2203, https://doi.org/10.1175/JPO-D-21-0264.1.

Van Roekel, L., and Coauthors, 2018: The KPP boundary layer scheme for the ocean: Revisiting its formulation and benchmarking one-dimensional simulations relative to LES. *Journal of Advances in Modeling Earth Systems*, **10 (11)**, 2647–2685, https://doi.org/10.1029/2018MS001336.

Wang, Q., C. Wekerle, S. Danilov, X. Wang, and T. Jung, 2018: A 4.5 km resolution Arctic Ocean simulation with the global multi-resolution model FESOM 1.4. *Geoscientific Model Development*, **11 (4)**, 1229–1255, https://doi.org/10.5194/gmd-11-1229-2018.

Wang, Q., and Coauthors, 2023: Impact of high resolution on Arctic Ocean simulations in Ocean Model Intercomparison Project phase 2 (OMIP-2). *Geoscientific Model Development Discussions*, **2023**, 1–46, https://doi.org/10.5194/gmd-2023-123.

Wunsch, C., P. Heimbach, R. Ponte, I. Fukumori, and the ECCO-GODAE Consortium Members, 2009: The global general circulation of the ocean estimated by the ecco-consortium. *Oceanography*, **22 (2)**, 88–103, https://doi.org/10.5670/oceanog.2009.41.

Yu, Y., H. Stern, C. Fowler, F. Fetterer, and J. Maslanik, 2014: Interannual variability of arctic landfast ice between 1976 and 2007. *Journal of Climate*, **27**, 227–243, https://doi.org/10.1175/JCLI-D-13-00178.1.

Zhang, J., and D. A. Rothrock, 2003: Modeling global sea ice with a thickness and enthalpy distribution model in generalized curvilinear coordinates. *Mon. Weather Rev.*, **131**, 845–861, https://doi.org/10.1175/1520-0493(2003)131⟨0845:MGSIWA⟩2.0.CO;2.